JGR Solid Earth

RESEARCH ARTICLE
10.1029/2022JB025738

Deciphering the Whisper of Volcanoes: Monitoring Velocity Changes at Kamchatka's Klyuchevskoy Group With Fluctuating Noise Fields

Peter Makus[1,2], **Christoph Sens-Schönfelder**[1], **Luc Illien**[1,3], **Thomas R. Walter**[1,3], **Alexander Yates**[4], **and Frederik Tilmann**[1,2]

[1]Helmholtz Center, German Research Center for Geosciences GFZ, Potsdam, Germany, [2]Institute for Geological Sciences, Freie Universität Berlin, Berlin, Germany, [3]Department of Geosciences, University of Potsdam, Potsdam, Germany, [4]University Grenoble Alpes, University Savoie Mont Blanc, CNRS, IRD, University Gustave Eiffel, Grenoble, France

Abstract Volcanic inflation and deflation often precede eruptions and can lead to seismic velocity changes (dv/v) in the subsurface. Recently, interferometry on the coda of ambient noise-cross-correlation functions yielded encouraging results in detecting these changes at active volcanoes. Here, we analyze seismic data recorded at the Klyuchevskoy Volcanic Group in Kamchatka, Russia, between summer of 2015 and summer of 2016 to study signals related to volcanic activity. However, ubiquitous volcanic tremors introduce distortions in the noise wavefield that cause artifacts in the dv/v estimates masking the impact of physical mechanisms. To avoid such instabilities, we propose a new technique called *time-segmented passive image interferometry*. In this technique, we employ a hierarchical clustering algorithm to find periods in which the wavefield can be considered stationary. For these periods, we perform separate noise interferometry studies. To further increase the temporal resolution of our results, we use an AI-driven approach to find stations with similar dv/v responses and apply a spatial stack. The impacts of snow load and precipitation dominate the resulting dv/v time series, as we demonstrate with the help of a simple model. In February 2016, we observe an abrupt velocity drop due to the M7.2 Zhupanov earthquake. Shortly after, we register a gradual velocity increase of about 0.3% at Bezymianny Volcano coinciding with surface deformation observed using remote sensing techniques. We suggest that the inflation of a shallow reservoir related to the beginning of Bezymianny's 2016/2017 eruptive cycle could have caused this local velocity increase and a decorrelation of the correlation function coda.

Plain Language Summary Before eruptions, volcanoes inflate due to the rising magma from below. Previous studies have found that these deformations can lead to small changes in the properties of the surrounding rock. We use passive image interferometry, a method that relies on the omnipresent background vibration of the Earth—mostly induced by the oceans, to measure these changes at the Klyuchevskoy Volcanic Group in Kamchatka, Russia. However, in Kamchatka, this background noise is masked and distorted by small earthquakes and tremors originating from the volcanoes themselves. We combine machine learning techniques with established monitoring methods to find times when these tremors remain similar. Afterward, we use data from these time periods in the conventional way to observe changes in the soil and the rock. Our results show that rain- and snowfall and the thickness of the snow cover exert the strongest influence on the properties of the rocks. Additionally, we found that a large magnitude 7.2 earthquake, which struck Kamchatka during our study, caused a slight weakening of the rocks due to microstructural damage. We register changes shortly before an eruption and suggest a connection to the beginning of an eruptive cycle in 2016.

Key Points:

- Fluctuating noise conditions lead to distortions in noise interferometry studies, which we avoid with the help of machine learning
- The seismic velocity on Kamchatka is affected by numerous mechanisms, amongst them environmental, tectonic, and volcanic events
- We observe a velocity increase at Bezymianny during February 2016 and link it to the beginning of the eruptive cycle

Supporting Information:

Supporting Information may be found in the online version of this article.

Correspondence to:

P. Makus,
makus@gfz-potsdam.de

Citation:

Makus, P., Sens-Schönfelder, C., Illien, L., Walter, T. R., Yates, A., & Tilmann, F. (2023). Deciphering the whisper of volcanoes: Monitoring velocity changes at Kamchatka's Klyuchevskoy group with fluctuating noise fields. *Journal of Geophysical Research: Solid Earth*, *128*, e2022JB025738. https://doi.org/10.1029/2022JB025738

Received 4 OCT 2022
Accepted 16 MAR 2023

Author Contributions:

Conceptualization: Peter Makus, Thomas R. Walter
Formal analysis: Peter Makus
Funding acquisition: Christoph Sens-Schönfelder
Investigation: Peter Makus
Methodology: Peter Makus, Luc Illien, Alexander Yates
Project Administration: Christoph Sens-Schönfelder, Frederik Tilmann
Software: Peter Makus

1. Introduction

1.1. Motivation for Noise Interferometry Studies at Active Volcanoes

For decades, if not centuries, scientists have been looking for methods to improve the accuracy and reliability of volcano eruption forecasts. They have done so utilizing a multitude of techniques from different disciplines. For example, satellite-born techniques (Mania et al., 2019; Massonnet et al., 1995) or tiltmeters (Fontaine et al., 2014; Peltier et al., 2005) can be used to detect topographic changes induced by inflation of the volcanic edifice. In many cases, increased seismicity also precedes eruptions (e.g., Budi-Santoso et al., 2013; Chouet, 1996; Droznin et al., 2015; Soubestre et al., 2021). However, the various precursors are differently pronounced from volcano to

Supervision: Christoph Sens-Schönfelder, Frederik Tilmann
Visualization: Peter Makus
Writing – original draft: Peter Makus
Writing – review & editing: Peter Makus, Christoph Sens-Schönfelder, Luc Illien, Thomas R. Walter, Frederik Tilmann

volcano and may not even occur at all, which emphasizes the need to explore other types of precursors (Brenguier et al., 2016; Brenguier, Shapiro, et al., 2008).

With the help of coda wave interferometry (Snieder, 2006), some authors demonstrated that changes in the seismic velocity (*dv*/*v*) often accompany the different stages of an eruptive cycle (e.g., Ratdomopurbo & Poupinet, 1995; Snieder & Hagerty, 2004). However, coda wave interferometry relies on repetitive sources with similar source-time functions, which limits the application to seismically active times and regions or requires expensive active source studies. Sens-Schönfelder and Wegler (2006) overcame this limitation by computing *dv*/*v* from ambient seismic noise using a technique called passive image interferometry (PII). Along with other factors, such as hydrological fluctuations (Clements & Denolle, 2018; Illien et al., 2021; Mao et al., 2022; Rodríguez Tribaldos & Ajo-Franklin, 2021), seasonal variations due to meteorological changes (Hillers et al., 2015; Sens-Schönfelder & Wegler, 2006; Wang et al., 2017), freezing-thawing cycles (Gassenmeier et al., 2014; James et al., 2019; Lindner et al., 2021; Steinmann et al., 2021), and earthquake-induced subsurface damages (Bonilla et al., 2019; Boschelli et al., 2021; Brenguier, Campillo, et al., 2008; Hobiger et al., 2016; Viens et al., 2018; Wegler et al., 2009; Wegler & Sens-Schönfelder, 2007), velocity changes due to volcanic inflation cycles have been detected by PII (Bennington et al., 2015; Brenguier, Shapiro, et al., 2008; De Plaen et al., 2016, 2019; Donaldson et al., 2017, 2019; Hirose et al., 2017; Machacca-Puma et al., 2019; Obermann, Planès, Larose, & Campillo, 2013; Olivier et al., 2019; Ruiz et al., 2022; Sens-Schönfelder et al., 2014).

However, PII is not only sensitive to changes in the medium but is also impacted by fluctuations in the noise wavefield (Hadziioannou et al., 2011). Such fluctuations are particularly problematic in active volcanic regions as pervasive volcanic tremors cause constant changes in the spatio-temporal distribution of sources and frequency content of the noise field. In contrast to other causes of noise field fluctuations, such as cultural noise, seasonal changes, or weather-induced changes, these fluctuations are hard to predict and often last for extended periods of days and months.

In this study, we propose and demonstrate a technique to mitigate the impact of these fluctuations that we found particularly effective in the case of ubiquitous volcanic tremors. After briefly outlining the trace stretching method, we discuss an approach that relies on machine learning to find time segments with temporarily stationary noise fields and describe a non-linear spatial stack that further reduces uncertainty in the *dv*/*v* estimates. In our *dv*/*v* results, we find influences of a multitude of tectonic, environmental, and volcanic processes. We further analyze these mechanisms by evaluating peak ground velocity/velocity change responses, developing a snow depth and precipitation *dv*/*v* coupling model, and discussing volcanic activity during the experiment. Finally, we draw some concluding remarks concerning our work's methodological novelties and geoscientific implications.

1.2. Kamchatka and the Klyuchevskoy Volcanic Group

Kamchatka is a peninsula situated in Russia's far east, west of the Aleutian Islands, and north of the Kuril Islands. Even though Kamchatka is located at a latitude of about only 60° N, temperatures can reach down to −40°C and remain low around the year. On Kamchatka's east coast, the annual precipitation can be up to 2,700 mm/yr. Together, these effects lead to thick snow covers for over 6 months per year, especially at higher altitudes (Hersbach et al., 2020).

The subduction of the Pacific Plate under the Okhotsk Microplate at a rate of about 80 mm/yr (Bürgmann et al., 2005) regularly causes large earthquakes, among them the magnitude 7.2 Zhupanov earthquake that struck on 30 January 2016 south of the study region (see Figure 1). The magmatic activity under Kamchatka has also been associated with this subduction. Despite its extraordinarily high productivity and almost constant activity, most of the volcanism on Kamchatka does not pose an immediate threat as the peninsula is only sparsely populated (Koulakov, 2021). However, eruptions may impact important aviation routes in the Western Pacific (Girina et al., 2019), and effects like ash clouds or tsunamis (Belousov et al., 2000) could reach far beyond Kamchatka's borders. Furthermore, knowledge gained from Kamchatka can be transferred to other volcanic systems posing threads for densely populated areas such as in Japan or Central and South America.

The Klyuchevskoy Volcanic Group (KVG) lies within the Central Kamchatka Depression (CKD) in central-east Kamchatka. While the KVG consists of dozens of volcanoes (see Figure 1), currently, only three of them are active: Bezymianny, Klyuchevskoy, and Tolbachik (Fedotov et al., 2010). During our study period, between the summer of 2015 and summer of 2016, Klyuchevskoy exhibited high seismic activity with intermittent eruptions.

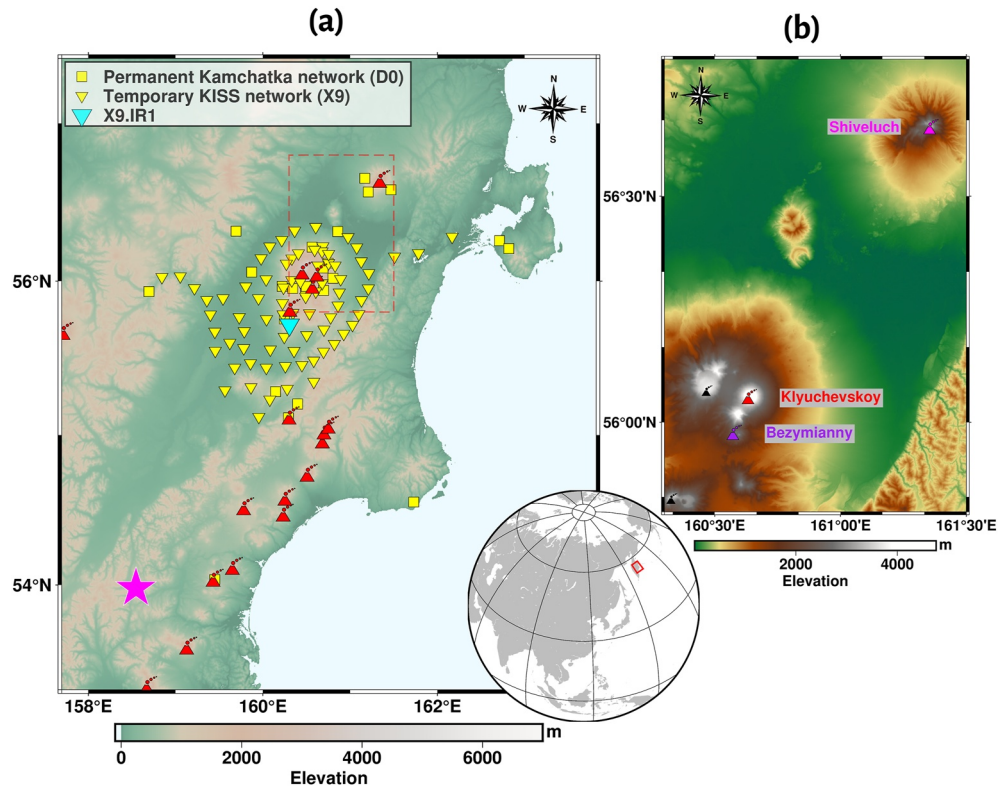

Figure 1. A map view of the study region. (a) The sites of permanent and temporary stations are represented by squares and triangles, respectively. We use data from station X9.IR1 (cyan) in Figures 2 and 3. The epicenter of the M7.2 Zhupanov earthquake is plotted as a magenta-colored star. We depict the locations of volcanic centers active during the Holocene. (b) A zoom on the area marked by the dashed, red box is shown in (a). The locations of the three volcanoes discussed here, Bezymianny, Klyuchevskoy, and Shiveluch are indicated and labeled.

In addition, Bezymianny showed signs of the initiation of an eruptive cycle, whereas Tolbachik remained inactive (Coppola et al., 2021; Journeau et al., 2022; Mania et al., 2021). Evidence from geophysical and petrological data suggests the existence of a common magma reservoir at about 30 km depth (Fedotov et al., 2010; Ozerov et al., 1997). However, the isotope composition of the magmas seems to contradict these findings (Dorendorf et al., 2000; Kayzar et al., 2014). The deeper magma reservoir feeds several complex systems of smaller shallow magma chambers at about 5 km depth and, in the case of Klyuchevskoy, directly into the volcano (Green et al., 2020; Journeau et al., 2022; Koulakov et al., 2017; Shapiro et al., 2017). Koulakov et al. (2021) proposed the existence of a separate gas-filled chamber responsible for Bezymianny's explosive activity. Recently, Coppola et al. (2021) showed that activities of Bezymianny and Klyuchevskoy are correlated, whereas activity at Tolbachik seems to reduce the output at the two other volcanoes indicating a complex, interconnected volcanic plumbing system.

A number of publications focused on the spatio-temporal evolution of volcanic tremors and volcano-tectonic events at the KVG. Volcanic tremors are thought to result from fluid movements and pressure variations in the volcanic plumbing system (Chouet, 1996). For Kamchatka, Soubestre et al. (2019) and Journeau et al. (2022) show that tremors occurring below several active volcanoes migrate periodically between shallow and deep locations. These tremors dominate the noise field above ~0.5 Hz (Gómez-García et al., 2018). As we will discuss later, this observation has important implications for noise interferometry studies.

Other studies have investigated the time-dependent variations of the subsurface properties. Koulakov et al. (2013) found velocity changes in the upper crust below the KVG using repeated 3D seismic tomography. They interpreted these changes as signs of magma migration preceding eruptive periods. However, due to its coarse temporal resolution, 4D earthquake tomography is only of limited use for eruption early warning. Gómez-García et al. (2018) applied PII to data collected at the KVG. While they recovered long-term velocity changes from frequencies

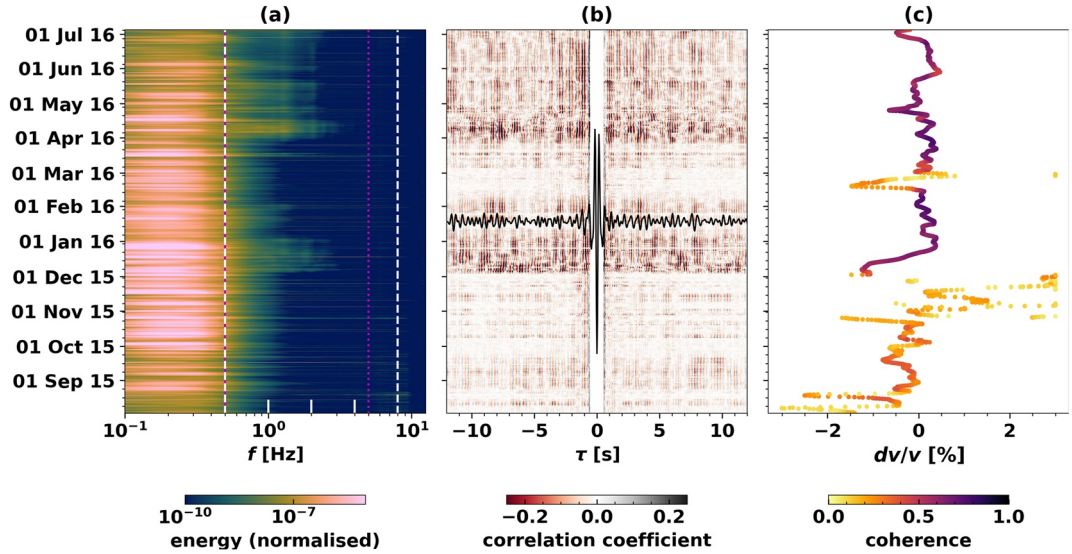

Figure 2. (a) Spectrogram of station's X9.IR1 N component calculated with a 4 hr window. Volcanic tremors appear as obvious bright (i.e., high energy) spots between ∼0.5 and 5 Hz (frequency band marked with magenta dotted lines). We truncated the color scale at both ends. In this work, we analyze velocity changes in octave bands between 0.5 and 8 Hz (marked by white dashed lines) (b) Daily self-correlation functions as calculated from station X9.IR1 between the E and N component created from preprocessed waveform data between 2 and 4 Hz. Note that the shape of the correlation functions (CF) (i.e., the Green's function estimate) changes significantly during the study. The average CF is plotted in black on top of the heatmap. We muted the daily correlation functions for $-0.5\ \text{s} \leq \tau \leq 0.5\ \text{s}$ to emphasize the shape of the coda. The color scale is truncated to −0.25 and 0.25, respectively. (c) The velocity change was estimated using the trace stretching method with the data from (b) and smoothing of 2 days. We indicate the location of X9.IR1 in Figure 1.

below 0.7 Hz, their algorithm showed limitations for higher frequencies due to strong fluctuations in the regional noise wavefield. *dv*/*v* time series retrieved from these lower frequencies are usually limited in their temporal resolution due to the high variability of the ocean-generated microseismic signals (e.g., weather and particularly storm dependence). Additionally, they are ill-suited to study shallow variations. In this study, we retrieve stable *dv*/*v* estimates for four one-octave-wide frequency bands between 0.5 and 8 Hz during shorter time segments by exploiting uniform noise fields that are temporarily stable and, thereby, obtain high-resolution *dv*/*v* time series that reveal fast-acting, shallow medium changes and their accurate timing.

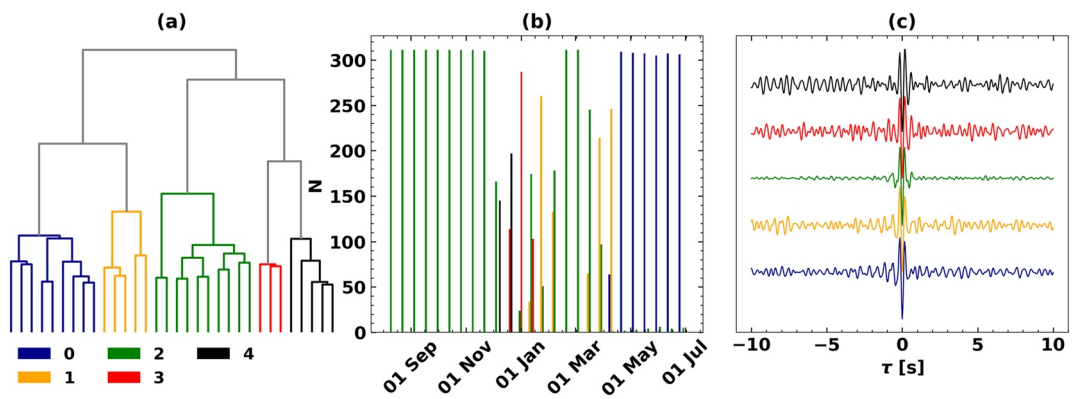

Figure 3. The output of the hierarchical clustering. As input data, we used 1 year of self-correlations between station's X9.IR1 (see Figure 1) east and north components created from waveform data between 2 and 4 Hz. Colors are used to identify the different clusters in the three panels. (a) A dendrogram that quantifies the similarity between the different clusters. The vertical distance of the branches scales with the dissimilarity of the clusters, that is, their merging cost (see Table S1 in Supporting Information S1). We show unclustered branches in gray. (b) The distribution of the clusters over the whole study period. The bars show the bi-weekly occurrence N of the respective cluster. (c) Averages of the correlation functions belonging to each of the five clusters.

2. Data and Preprocessing

2.1. Seismic Data

For this study, we use 1 year of seismic data from 101 broadband and short-period stations (Figure 1). Of these, 77 are part of the temporary KISS deployment (Shapiro et al., 2017) between summer 2015 and summer 2016. The remaining 24 stations are permanent stations operated by the Kamchatka Branch of the Geophysical Survey of the Russian Academy of Sciences.

Before computing cross- (i.e., inter-station), self- (i.e., inter-component, see Hobiger et al. (2014)), and auto-correlations, we apply some common preprocessing steps to the seismic data: First, we load daily chunks of data that we subsequently downsample to 25 Hz, detrend, taper, and filter in octave wide passbands. For cross- and self-correlations, but not for auto-correlations, we whiten the spectrum in the frequency domain (i.e., dividing the traces' spectra by their amplitude spectra). We discard the traces' amplitude information while only keeping its sign (i.e., one-bit or sign-bit normalization), which we found to be the most effective way to mitigate the impact of high amplitude sources for our data. Afterward, we slice the data into 1-hr-long windows and compute correlation functions (CFs) in the Fourier domain. Finally, we obtain a $J \times T$ matrix per component combination, where J is the number of hourly correlations and T is the number of time samples. We store these in the time domain.

Finally, to retrieve our velocity change estimates, we apply the trace stretching technique (Sens-Schönfelder & Brenguier, 2019; Sens-Schönfelder & Wegler, 2006). First, we select N subsets of all CFs (for details, see Section 3.3). From these subsets, we stack four-hourly noise correlations ξ_j every 2 hrs (i.e., we smooth with a moving mean) to reduce random noise in the CFs. In the stretching method, one stretches a reference trace against all these traces. We use the mean of all J_n CFs in one subset as reference ξ_r:

$$\xi_r = \sum_{1}^{J_n} \frac{\xi_j}{J_n} \tag{1}$$

The algorithm performs a grid search over I stretching (or compression) factors κ_i to find the one resulting in the highest correlation coefficient R between ξ_j and ξ_r:

$$R_{i,j} = \int_{\tau_1}^{\tau_2} \xi_j(\tau)\xi_r(\tau(1+\kappa_i))\mathrm{d}\tau \tag{2}$$

For homogeneous velocity changes, $(dv/v)_j = -\kappa_{\max,j}$, where $\kappa_{\max,j}$ is the stretching factor resulting in the maximum correlation coefficient at time step j. We perform the grid search for $-0.025 \leq \kappa \leq 0.025$ (i.e., up to 2.5% deviation from the reference velocity) and coda times where the lag time is between $\tau_1 = 7.5T_1$ and $\tau_2 = 17.5T_1$ relative to the theoretical time of arrival, on both causal and acausal parts of the CF. T_1 corresponds to the long period corner period of the applied bandpass filter (Hobiger et al., 2014); for auto- and self-correlations, the reference time is accordingly 0. In the stretching method, the maximum correlation coefficient $\max(R_j)$ additionally serves as a stability measure of the retrieved velocity change estimates. Ultimately, we retrieve N *similarity matrices* of the size $I \times J_n$ that relate the correlation coefficient R to the four-hour-long time sample j and the stretching factor κ. For each similarity matrix, we thus obtain a velocity change estimate time series $(dv/v)_j$.

To execute these steps, we employ SeisMIC (Makus & Sens-Schönfelder, 2022), a freely available open-source software suite written in Python. SeisMIC is available on GitHub and will be discussed in detail in a separate publication.

2.2. Complementary Data

To set our results in context to potential environmental and volcanological forcing, we retrieve snow load, precipitation, and temperature data from ERA5, a global climate reanalysis dataset. ERA5 is sampled every hour and is resolved on a 9×9 km grid (Hersbach et al., 2020). While the precipitation data shows degraded accuracy on an hourly time scale (Tang et al., 2020), its performance is still sufficient for our purposes. For Kamchatka, ERA5 is exclusively based on satellite data.

We rely on infrared satellite measurements (Coppola et al., 2021) to compare the determined velocity changes to the lava output of the volcanoes.

The magnitudes and origin times for regional earthquakes were obtained from the USGS FDSN web service.

3. Stabilizing Velocity Change Estimates

3.1. The Limitations of Passive Image Interferometry in Fluctuating Noise Fields

Ideally, each of our J CFs would correspond to a Green's function approximation at the time t_j. In practically all cases, however, non-uniform noise fields violate this assumption. While noise interferometry does not require an actual Green's function approximation, a stationary noise field is necessary for the study to succeed (Hadziioannou et al., 2011). Commonly, researchers apply a set of standard preprocessing techniques such as those described in Section 2 to mitigate the impact of this non-stationarity directly in the data (Fichtner & Tsai, 2019). Another standard approach is the temporal smoothing of CFs, which results in a trade-off between stability and temporal resolution. This approach assumes that rapid fluctuations between CFs retrieved from the noise of consecutive times are due to the stochastic character of the noise and, hence, can be reduced by temporal smoothing. Processing the dv/v observations can improve the monitoring further. Even though these steps aim to reduce the measurement noise, we try to avoid the term denoising as we find it ambiguous in the context of ambient noise seismology. Instead, we prefer the broader term *stabilization* of CFs and dv/v estimates.

For data from Kamchatka, Gómez-García et al. (2018) have already shown that standard preprocessing does not suffice to retrieve stable dv/v estimates. They proposed a different algorithm that exploits a Bayesian framework to estimate dv/v. However, their algorithm shows limitations for higher frequencies severely impacted by the pervasive fluctuation of volcanic tremors (see power spectrum in Figure 2a). In addition, the proposed method is not suited to retrieve reliable long-term trends when properly parametrized for changing noise fields (Gómez-García et al., 2018). To illustrate the non-stationarity of the CFs, we show the east-north component of the self-correlation matrix of station X9.IR1 in Figure 2b. When the energy is high (e.g., December 2015), the corresponding CFs differ from other times. Journeau et al. (2022) showed that the intensity of the tremors fluctuates simultaneously, confirming that volcanic sources cause the changes in noise amplitudes and CFs. For illustrative purposes, we show a velocity change estimate using the standard trace stretching approach in Figure 2c. The resulting dv/v fluctuates strongly with abrupt changes in the associated correlation coefficient (i.e., the coherence), indicating that this measurement does not reflect physical changes in the subsurface and cannot be interpreted. Interestingly, the dv/v estimate has the highest correlation coefficient when volcanic tremors dominate the noise field. Hence, it seems as if phases that emerge in the CFs due to the high-energy tremor dominate the reference CF, which is a mean of all CFs.

3.2. Previous Approaches

Aside from standard preprocessing and Bayesian-type inversions (Gómez-García et al., 2018), several methods have been proposed to avoid instabilities due to non-stationary wavefields. Hadziioannou et al. (2011) utilized an adaptive filter to remove incoherent phases from CFs. Moreau et al. (2017) combined singular value decomposition with a Wiener filter to remove statistically and linearly independent components from the CFs. Schimmel et al. (2011) computed CFs using a phase cross-correlation rather than a conventional cross-correlation to suppress the impact of non-coherent high-amplitude phases. Viens and Van Houtte (2020) implemented an approach that employs deep learning to remove incoherencies from CFs. Most of these solutions yield good results for noise that remains constant over the whole study period and distorts all CFs more or less equally. However, when the ambient wavefield changes entirely due to a shift of dominant sources over long periods, they become ineffective. In Kamchatka, volcanic tremors can last and remain stable for several months (Journeau et al., 2022; Soubestre et al., 2019), so we require a different approach to achieve stable dv/v estimates from ambient noise.

Recently, there has been a shift from more traditional filtering methods to methods using machine learning algorithms. Arguably the most popular choices among these are unsupervised clustering algorithms and unsupervised de-mixing algorithms. Both are particularly well-suited for large amounts of continuous data as they occur in ambient noise seismology. For example, Seydoux et al. (2020) clustered raw waveform data to differentiate ambient noise from earthquake signals. Similarly, Steinmann, Seydoux, Beaucé, and Campillo (2022) combined independent component analysis (ICA), a dimensionality reduction algorithm that separates statistically independent features, with hierarchical clustering. Thereby, they succeeded to discriminate time windows with different dominant sources. In another approach, they analyzed the output features of the ICA and found a feature that closely resembles the velocity change of the medium (Steinmann, Seydoux, & Campillo, 2022). While this approach seems to retrieve very accurate and highly resolving dv/v estimates for their dataset, one must have

successfully retrieved a low-resolution baseline estimate of *dv*/*v* using a conventional algorithm. Only then it is possible to evaluate that a feature of the decomposition corresponds to *dv*/*v* and provide quantitative estimates of the velocity change, as the amplitude of the ICA coefficients is physically meaningless. These limitations reduce the applicability of the ICA-based method. In addition, in more complex datasets, like our datasets, *dv*/*v* does not seem to be confined to a single feature of the ICA decomposition rendering the output practically uninterpretable. A more general issue with approaches that rely entirely on machine learning is that the related physical processes remain elusive, often making a correct interpretation of the results challenging. In the following section, we will describe an approach that combines the advantages of machine learning and conventional noise interferometry to retrieve velocity change estimates for the Kamchatka dataset.

3.3. Clustering Noise Correlations

We address the varying noise conditions by splitting the experimental period into segments during which the ambient field is sufficiently stationary to observe temporal changes in the subsurface material. By clustering the CFs, we identify moments of change in the noise field that naturally separate the different segments. We use an agglomerative hierarchical clustering algorithm employing Ward's linkage algorithm with a Euclidean distance metric that minimizes the variance in each cluster (Ward, 1963) to find CFs that are sufficiently similar to be used in the same interferometric analysis. For many clustering algorithms, such as K-means clustering, the user determines the number of clusters before assigning the data to these clusters. Hierarchical clustering, in contrast, returns a dendrogram representing possible clusters and subclusters and their respective (dis-)similarities (Müllner, 2013). Thereby, it helps avoid an unsuitable choice of cluster numbers that would result in poorly defined clusters or too few clusters lumping together members with large differences. For a detailed discussion of the hierarchical clustering of noise correlations, refer to Yates et al. (2022).

Similar to Yates et al. (2022), we cluster preprocessed CFs instead of raw waveform data to disregard factors such as amplitude variations in the ambient noise irrelevant to our study. Additionally, the cross-correlation serves as a dimensionality reduction that reduces the computational cost of the clustering. Instead of clustering CFs from all stations, we only use self-correlations from station X9.IR1 and component combination N-E that is sensitive to body, Love, and Rayleigh waves. As changes in the wavefield are regional, we do not obtain markedly different clusters for other stations and combinations (see Figure S7 in Supporting Information S1). Also, using separate clusters would unnecessarily complicate the comparability of results between different stations.

We show the hierarchical dendrogram for data between 2 and 4 Hz in Figure 3a. As a compromise between stability and length of the *dv*/*v* time series, we split the dataset into five clusters. For 2–4 Hz, all clusters are highly dissimilar with a minimum cluster merging cost of about 9 (see Table S1 in Supporting Information S1 for a merging cost-frequency overview).

We can assess the nature of each cluster by examining its temporal occurrence (see Figure 3b) and the shape of its average CF (Figure 3c). Most average CFs share some common features at early lag times, but their peaks differ later in the coda, confirming that they are ill-suited for an interferometry study based on a single reference trace and time window. Remarkably different from all other average CFs is group number 2 (green), which dominates during times of low volcanic activity. When comparing the temporal distribution of the clusters (Figure 3b) to the volcanic tremor activity found by Journeau et al. (2022), it becomes evident that they directly correspond to the different dominating sources. During periods of low volcanic activity, cluster 2 (green) dominates. Clusters 3 and 4 correspond to periods at which volcanic tremors prevail. During the eruption at Klyuchevskoy volcano starting in April 2016, cluster 0 becomes active.

For the clustering, we focus on CFs created from the frequency band between 2 and 4 Hz, which shows the greatest impact of volcanic tremors (see Figure 2a). However, we remark that almost all frequency bands, particularly above 2 Hz, show similar patterns as the one under discussion, albeit not always as pronounced. Below 0.25 Hz, we find no temporal patterns attributed to volcanic activity. We provide additional clustering results in Figures S1-S7 in Supporting Information S1.

To retrieve stable *dv*/*v* estimates for shorter periods, we apply the trace stretching algorithm to *all CFs* in time periods dominated by one (e.g., August 2015 to November 2015, April 2016 to July 2016, see Figure 3b) or, in some cases, two clusters (time windows at the turn of the year, see Figure 3(b)). Thus, instead of using CFs from only one cluster per *dv*/*v* estimation, we use all CFs for a given period. Applying interferometry to only one

cluster could introduce a bias if the clustering algorithm splits the dataset due to changes in the medium (i.e., stretching of the CF), which we want to retain and analyze in PII, rather than changes in noise characteristics. For a much longer continuous dataset at Piton de la Fournaise, Yates et al. (2022) show that changes in the medium alter the dominant cluster permanently, whereas changes in the noise wavefield only lead to temporary variations. However, for the times available to us at KVG, making such an evaluation is challenging since varying tremors, which commence in late November 2015, last throughout the whole study period (Journeau et al., 2022).

For each period, we use the average CF as a reference correlation function to measure changes in wave velocity. The same segments are chosen for all stations and station groups. In the following, we will refer to our described method as *time-segmented passive image interferometry (TSPII)*. We provide a complete overview of the chosen time segments in Table S2 in Supporting Information S1.

An obvious drawback of TSPII is that it fails to track long-term changes of dv/v. Gómez-García et al. (2018) used data from lower, less tremor-affected frequencies to compute long-term velocity changes. For higher frequencies, however, the modifications in the noise wavefield will induce changes in the spatial sensitivity between the subsequent time segments. Therefore, the time segments quantify dv/v in different locations and they cannot be set in context to each other.

3.4. Spatial Stacking of Sequenced dv/v Time Series

Applying PII to the selected time windows yields several dv/v time series, of which many show a significant amount of fluctuations that we regard as measurement noise. One strategy to stabilize the measurements is to apply smoothing in the time domain, as is commonplace in PII studies. In our case, however, this would degrade the time resolution and limit the usefulness of the already relatively short dv/v time series resulting from the time segmentation.

Statistical noise in dv/v measurements can be reduced by applying spatial stacking over results from several stations (Illien et al., 2023). We stack the similarity matrices that the trace stretching algorithm yields (see Equation 2). Subsequently, we pick the location of the maxima on the stacked similarity matrix to find the apparent homogeneous velocity change. In comparison to directly averaging the dv/v time series, this strategy has the advantage that unstable estimates with low correlation coefficients are down-weighted. On the flip side, the non-linear nature of the stack makes it challenging to quantify uncertainties and the contribution of different areas to the obtained velocity changes. Due to the ergodic nature of ambient seismic noise, one faces a decision between temporal and spatial resolution by opting for a more aggressive smoothing in either domain to reach the same stability (Illien et al., 2023). As we are looking for rapid responses of the subsurface to volcanic processes in rather short dv/v time series, we opt for a high resolution in time rather than in space with 2-hr increments and 4-hr smoothing windows. We point out that the stacked correlation coefficient will almost always be lower than the correlation coefficient found from individual stations. To make a clear distinction between the two, we refer to the stacked correlation coefficient as the *cumulative correlation coefficient* (CCC).

When stacking similarity matrices, we need to find sites with similar velocity changes. Due to significant variations in topography and geology from site to site, these are not necessarily stations that are laterally closest to each other. To identify such stations, we employ an approach that combines visual inspection of the individual dv/v time series and a sequencing algorithm. Visually, we find that stations with a similar elevation and similar geology have similar dv/v curves for all examined frequencies (i.e., 0.5–8 Hz). To confirm this impression with an AI approach free of human bias, we use the TheSequencer algorithm (Baron & Ménard, 2021), which, in contrast to Ward's linkage algorithm, can quantify the distance between multidimensional data points (i.e., matrices). We chose the similarity matrices of each self-correlation from time segment 1 July 2015–1 December 2015 as our input data points. The algorithm then uses the Kullback–Leibler divergence and the Euclidean distance between the data points to find how the data is distributed in an N-dimensional space and sorts them by their respective distance. The closer two given data points are in said sequence, the more similar they are. We visualize the output of the algorithm in Figure 4a. As one should expect, results from correlations from different component combinations of the same station are close in the sequence in almost all cases (in the plot, circles on top of each other). Furthermore, the algorithm reveals a very similar pattern to our qualitative evaluation; it evaluates responses of stations around the KVG with high elevation as similar, whereas stations in the Central Kamchatka Depression (CKD), the regional sedimentary basin, and on the eastern ridge (ERidge) plot in different groups. Based on the resulting sequence, we decided to stack similarity matrices in the five groups shown in Figure 4b.

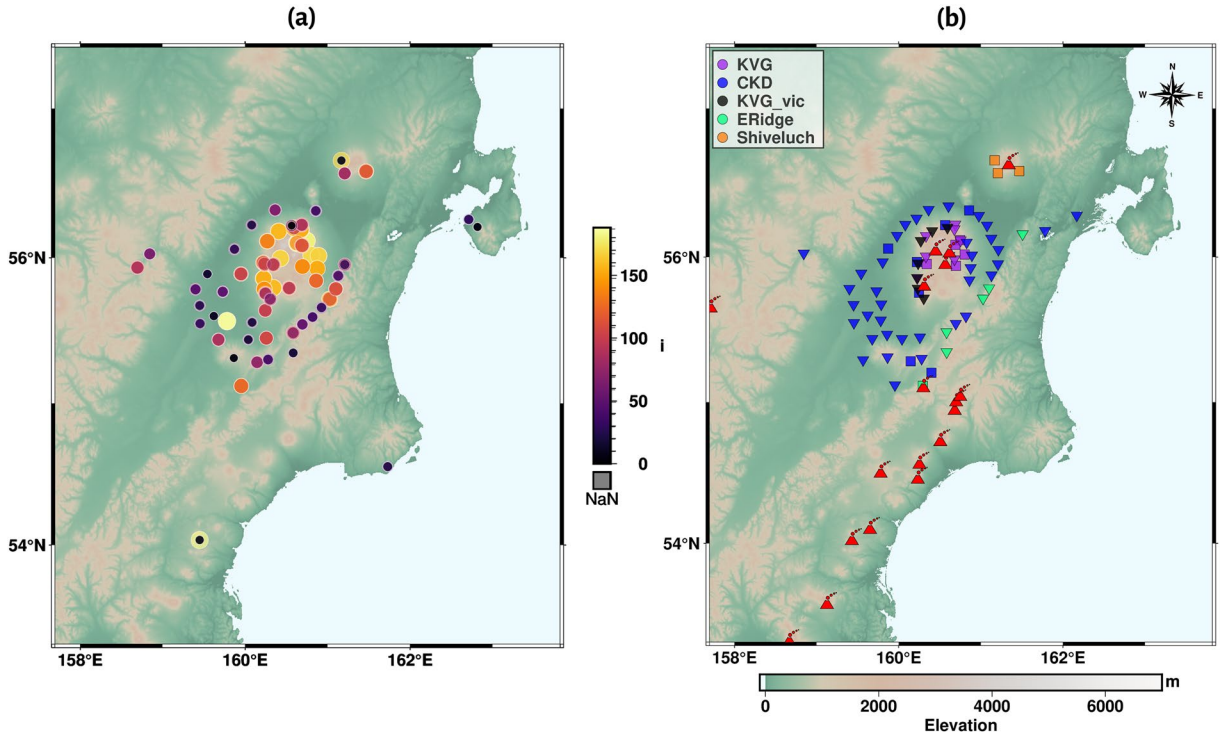

Figure 4. (a) The output of TheSequencer (Baron & Ménard, 2021). The closer two datapoints are in the sequence (i.e., similarly colored and similarly sized circles). the more similar the algorithm deemed their *dv/v* responses as given by the similarity matrices. Note that datapoints in the sedimentary basin, on the Klyuchevskoy Volcanic Group, and on the ridge in the East tend to build subgroups. (b) Groups that we use for spatial stacking. Based on the results shown in panel (a) and on visual inspection of the *dv/v* time series, we divide our dataset into five subgroups. Each color corresponds to a different subgroup. Inverted triangles represent stations belonging to the temporary KISS experiment, whereas squares are the locations of permanent stations. Note that we disregard some stations due to low data availability. We depict the locations of volcanic centers active during the Holocene. KVG: Klyuchevskoy Volcanic Group, CKD: Central Kamchatka Depression, ERidge: Eastern Ridge, KVG_vic: stations in the vicinity of the KVG.

4. Velocity Changes at the KVG

Using the method outlined above, we compute *dv/v* time series stacks for frequencies above 0.5 Hz, where volcanic tremor energy is generally very high (see Figure 2a). For frequencies below 0.5 Hz, the statistical variation exceeds the amplitude of physical velocity changes over 1 year, even after introducing an aggressive temporal smoothing with a window length of 30 days. To remove these statistical variations and obtain interpretable results from these frequencies, we would require a longer continuous dataset. The most stable results were obtained from the averages of auto- and self-correlations of all components from the stations of each of the groups shown in Figure 4.

Figure 5 shows the estimated velocity variation for the station group CKD from July 2015 to December 2015 for 4–8 Hz. We set these in context to precipitation, snow depth, and large regional earthquakes. In addition, we provide the time-averaged lava discharge rate (TADR) for Klyuchevskoy and Bezymianny that Coppola et al. (2021) estimated from satellite data. Most notably, we can see a significant temporal correlation between precipitation events and drops in seismic velocity (e.g., in early September), followed by periods of velocity recovery. When precipitation comes in the form of snow (i.e., is accompanied by an increase in snow load) as on 19 October (feature 1, marked by an arrow), decorrelations (i.e., decreases in the CCC) occur. From late October, the temperatures remain below freezing, and the snow load increases. Simultaneously, *dv/v* exhibits an almost monotonously increasing trend. For most earthquakes, we identify no correlated changes in *dv/v* - except for an event on 18 September that seems to be accompanied by a slight velocity increase (feature 2, cf. Section 5.2 for a thorough discussion of the impact of seismic events on *dv/v*). We do not identify any correlation between the seismic velocity and the TADR in Figure 5 or any of the following figures.

Similarly to Figure 5, we show a selection of *dv/v* results, climatological, and volcanological data from a set of groups and time windows in Figure 6, but for 2–4 Hz. As before, we note velocity reductions at times with high

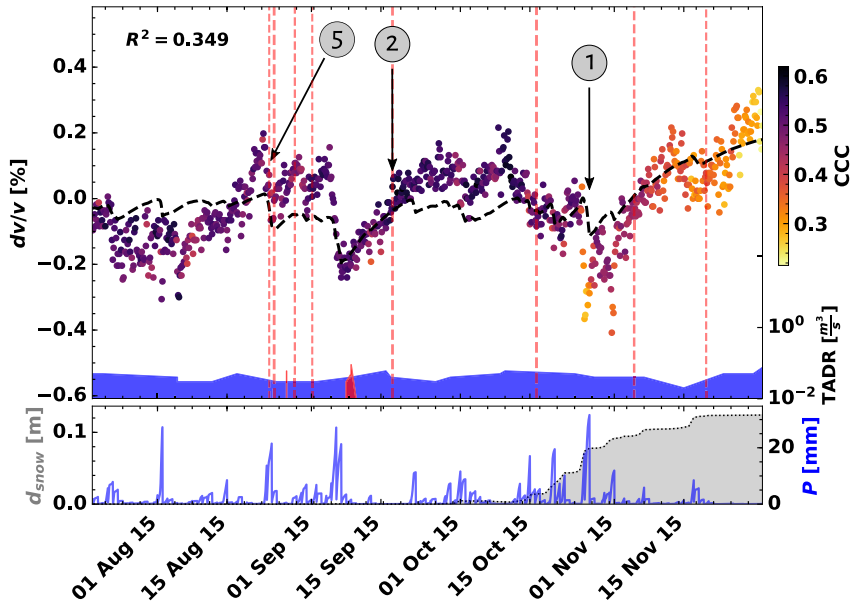

Figure 5. Velocity change for the station group CKD (see Figure 4) created from auto- and self-correlations between all components for 4–8 Hz. We show *dv*/*v* estimates as circles with color scaling dependent upon the cumulative correlation coefficient (CCC; see text body for details). Each point represents a time window of 4 hrs, at 2 hrs intervals. Red dashed lines mark the origin times of regional earthquakes with magnitudes ≥4.8. The *dv*/*v* model is given by the black dashed line, and the corresponding coefficient of determination (R^2) is shown in the upper left corner of the large tile. The time-averaged lava discharge rates (TADR) for Klyuchevskoy and Bezymianny are plotted logarithmically at the bottom of the plot in red and blue, respectively (Coppola et al., 2021). In the small tile below, we show values for snow depth d_{snow} (gray) and hourly precipitation P (blue) averaged over the region. Both values are given in water-equivalent. Note that, particularly for these high frequencies, *dv*/*v* shows strong responses to changes in precipitation and snow load. Our *dv*/*v* model (see Section 5.1.1) is able to reproduce these changes on first order. Features 1, 2, and 5 marked with arrows are discussed in the text body.

precipitation (e.g., Figure 6d feature 3). In Figures 6b and 6c, and 6d, we find that the velocity reductions over the respective periods coincide with a decrease in snow load, whereas, in Figure 6a, both snow load and velocity show an increasing trend. While these weather-driven effects are less obvious on inter-station correlations, they are nonetheless visible (see Figures S28-S45 in Supporting Information S1). In Figure 6c, we see a low correlation coefficient at the beginning of the time window, which coincides with the change in noise source dominance reflected by a shift from cluster 1 to 0. Consequently, we attribute it to an effect introduced by a change in wavefield properties. On 30 January 2016, the Magnitude 7.2 Zhupanov earthquake struck Kamchatka south of the network. Simultaneously, a sharp velocity decrease occurred at almost all station groups and frequencies (see Figure 6a feature 4). We show a more extensive selection of *dv*/*v* results for various time windows, frequencies, and regions in Figures S10-S45 in Supporting Information S1, including results from cross-correlations (i.e., inter-station). In the following section, we elaborate on the hydrological, meteorological, seismic, and volcanic forcing that causes velocity changes and discuss the impact of each respective mechanism on the different study sites.

5. Discussion of Physical Mechanisms Causing Velocity Changes

After demonstrating how velocity changes can be computed from data with challenging noise conditions and noting that the *dv*/*v* variations exhibit strong correlations to weather data, we discuss physical mechanisms related to meteorological events, seismic events, and volcanic events that induce or could induce the observed *dv*/*v* variations and, in particular, have a closer look at velocity changes that do not coincide with precipitation or changes in the snow cover. The impact on *dv*/*v* of these mechanisms has been reported by other studies before. Observing them with our method gives confidence that the *dv*/*v* time series resulting from TSPII are sufficiently robust to contribute to environmental and volcanological monitoring.

Since we focus on velocity changes obtained from frequencies >2 Hz and examine earlier parts in the coda, we mainly interpret velocity changes down to about 350 m (Obermann et al., 2016; Obermann, Planès, Larose,

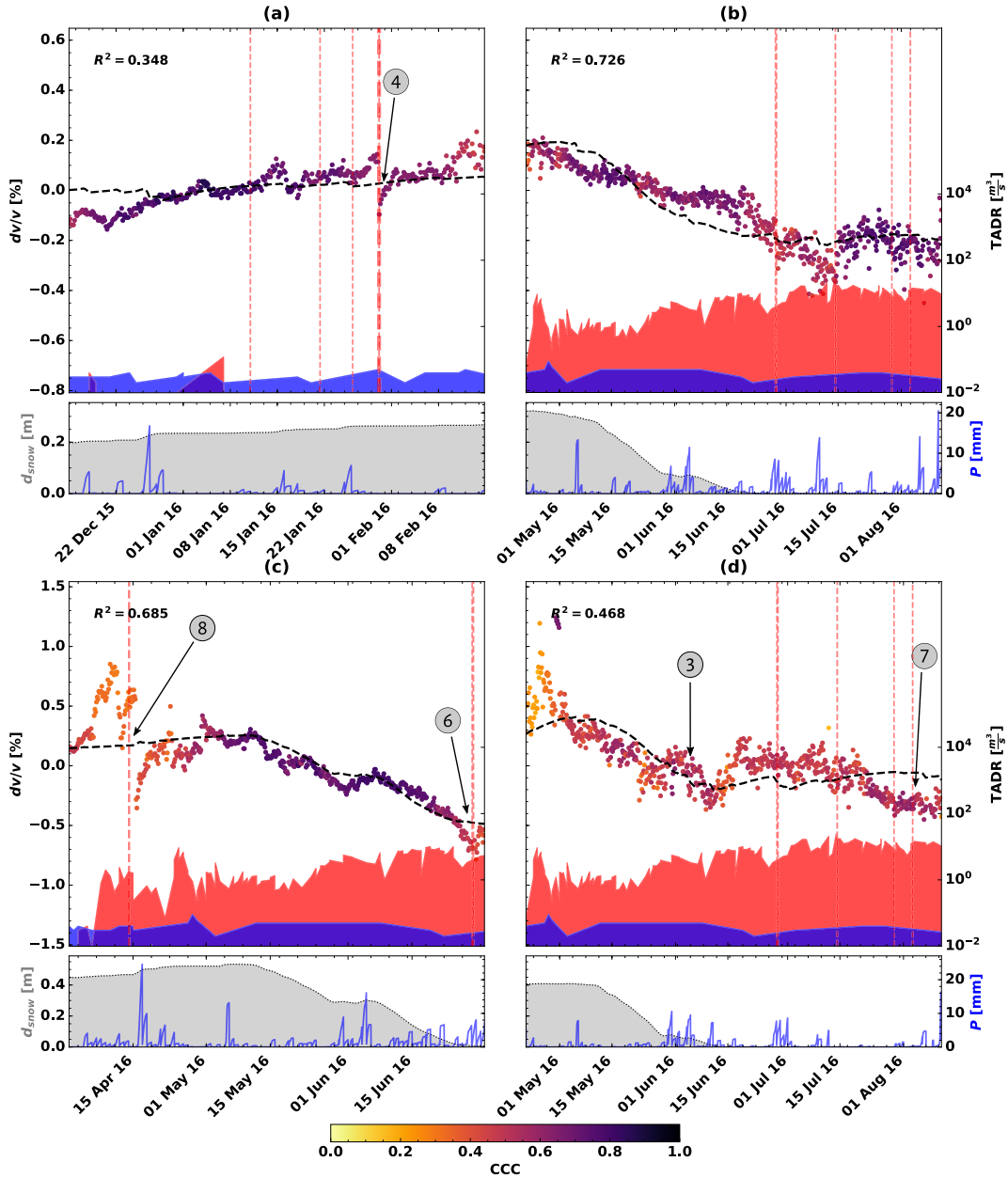

Figure 6. Velocity change estimates for different station groups and time intervals for 2–4 Hz. Refer to Figure 5 for an explanation of the plot's details. (a) Region KVG_vic, time window from 15 December 2016 to 15 February 2016. Bold dashed line marks the 30 January 2016 M7.2 Zhupanov earthquake. (b) Region CKD, time window from 22 April 2016 to 1 September 2016. (c) Region KVG, time window from 1 April 2016 to 1 July 2016. (d) Region Shiveluch, time window from 22 April 2016 to 1 September. Locations of the stations belonging to each of the regions can be found in Figure 4(b).

Sens-Schönfelder, & Campillo, 2013), assuming a surface wave velocity of 1 $\frac{km}{s}$ (Green et al., 2020). Surface waves of the lowest analyzed frequency of 0.5 Hz are sensitive to velocity changes down to about 1,300 m.

5.1. Climatic and Meteorological Variations on Kamchatka

In Section 4, we already denoted a clear anti-correlation between precipitation and dv/v. Such an anti-correlation has been observed since the dawn of PII and was explained by an increased pore pressure resulting in a reduction of the shear wave velocity v_S (e.g., Andajani et al., 2020; Donaldson et al., 2019; Feng et al., 2021; Wang et al., 2017).

As we examine high frequencies, we are particularly sensitive to changes in the shallow subsurface (Obermann, Planès, Larose, Sens-Schönfelder, & Campillo, 2013), which contains the vadose zone that is constantly subject to groundwater recharge and drainage cycles resulting in the observed velocity drop and recovery patterns.

However, in our case and for other observations in temperate and cold environments, this mechanism can only explain precipitation in the form of rain. In large parts of the year (i.e., approximately between October and May), temperatures are below-freezing. Consequently, precipitation occurs as snowfall, leading to the accumulation of a compacting snow layer. This added layer would alter the scattering properties of the medium in addition to the induced shear wave velocity change and, consequently, introduce a decorrelation (Guillemot et al., 2021; Obermann, Planès, Larose, & Campillo, 2013) as observed after periods of heavy snowfall (e.g., Figure 5 feature 1).

Guillemot et al. (2021) observed velocity drops, which they attributed to the build-up of a low-density and low-rigidity snow layer. In contrast to them, we see clear signs of a positive long-term correlation of overall snow load with dv/v (cf. Hotovec-Ellis et al., 2014; Mordret et al., 2016; Wang et al., 2017). In our case, the relationship appears remarkably linear aside from the previously discussed immediate effects of snowfall. We explain the relationship by invoking a loading mechanism, that is, an increased surface loading due to the snow mass (Heki, 2001; Silver et al., 2007) that results in a pore space reduction and closure of cracks leading to compaction of the snow and soil layers. In addition, the snow and ground frost might act as a seal that blocks groundwater recharge. Conversely, during spring, the seismic velocity decreases rapidly due to a decrease in load and groundwater recharge from meltwater and an associated opening of cracks (Gassenmeier et al., 2014; Guillemot et al., 2021). While most studies find that the velocity increases with increasing snow load, Taira and Brenguier (2016) observed a velocity decrease, which they explain by an increase in pore fluid diffusion.

5.1.1. Modeling dv/v

We use snow load and precipitation to create a simple model for the evolution of the seismic velocity at the various sites. In our model, dv/v depends bilinearly on the two environmental parameters. We express dv/v as:

$$\left(\frac{dv}{v}\right)_{syn} = aP * f(\tau) + bd_{snow} + C \tag{3}$$

where P is the precipitation in m (water equivalent), d_{snow} is the snow thickness in m (water equivalent), and a, b, and C are constants that we determine for each of the four octave frequency bands between 0.5 and 8 Hz and each station group. Akin to Sens-Schönfelder and Wegler (2006) and Hillers et al. (2014), we define a filter function $f(\tau)$ that we convolve (denoted as *) with the precipitation to model the drainage after each precipitation event. We define $f(\tau)$ in agreement with Darcy's law as a decaying exponential function that varies between 1 and 0:

$$f(\tau) = \begin{cases} 0 & \forall \tau \in (-\infty, 0) \\ \exp^{-\tau/\lambda} & \forall \tau \in [0, \infty) \end{cases} \tag{4}$$

where τ is the lag time (i.e., the time that has passed since the precipitation event) and λ is the decay.

To invert for a, b, C, and λ, we employ a least-squares inversion that optimizes a cost function to minimize the misfit between dv/v_{syn} and dv/v. For a and b, we jointly invert for all time windows using data from one station group and each octave frequency band. For the offset C, we perform a separate inversion for each time window. We determine λ to be optimal for the whole dataset at $\lambda = 10$ days. As expected, the magnitudes of a and b are higher for 2–8 Hz than for lower frequencies indicating that precipitation and snow load have a higher impact on the velocity of shallower layers. We do not identify clear trends in a and b for the different station groups (see Figure S8 in Supporting Information S1).

We show dv/v_{syn} as a black dashed line in Figures 5 and 6. Additionally, we provide the coefficient of determination R^2 for each time window as an objective measure to evaluate the fit of our model. R^2 reaches a value of 1 for a perfect fit, $R^2 = 0$ implies that the model has the same fit as the mean of the data points, and values below 0 have a fit worse than the mean. We achieve the highest R^2 values for times dominated by strong precipitation and changes in snow load (e.g., Figures 6(a) and 6(b), and (c), whereas, for dv/v curves that are strongly affected by mechanisms that our model does not take into account (e.g., earthquake damage, Figure 6), we obtain lower R^2 values.

Despite its simplicity, our model reproduces first-order trends of the dataset reliably. For lower frequencies between 0.5 and 2 Hz, it generally performs worse with R^2 values around 0 than for the higher frequencies, prob-

ably due to higher scatter in the *dv*/*v* datapoints in those low-frequency velocity change estimates (see Figures S10-S45 in Supporting Information S1). In addition, estimates from lower frequencies are not affected much by environmental mechanisms. Instead, lower frequencies sample deeper parts of the medium (Obermann, Planès, Larose, Sens-Schönfelder, & Campillo, 2013) whose velocity is not as strongly influenced by meteorological events (Donaldson et al., 2019). During times with relatively constant snow load, the model underestimates the velocity increase leading to lower R^2 values (see Figure 6a and Figures S10-S45 in Supporting Information S1) potentially because we do not model snow compaction.

We could increase the fit of our model by adding the influence of non-environmental effects such as ground shaking, employing separate models for rain and snowfall, adding the influence of snow compaction, utilizing a more complex model for snow layer thawing that accounts for the sudden availability of melt water, or taking thermal stress into account (Hillers et al., 2015). However, the model accuracy is limited by (a) the limited spatial resolution of satellite weather data (Tang et al., 2020) as ground measurements are unavailable to us and (b) the fact that we compare linear stacks of environmental data with non-linear stacks of *dv*/*v* measurements. The latter factor becomes especially important when the temperature is close to freezing or thawing so that freezing, snowfall, rain, and thawing could occur out of phase at stations belonging to one group of stations.

5.2. Impact of the 30 January 2016 Zhupanov Earthquake

Due to the subduction of the Pacific Plate below Kamchatka (Yogodzinski et al., 2001), the region is regularly shaken by large earthquakes, which are generally known to induce velocity changes (e.g., Brenguier, Campillo, et al., 2008). In our results (Figures 5 and 6, and Figures S10-S45 in Supporting Information S1), we show the origin times of regional earthquakes with magnitudes larger than 4.8. For most of these events, the impact on *dv*/*v* remains either unclear due to coincident events of precipitation (e.g., Figure 5 - feature 5 or feature 6 in Figure 6c) or vanishes below the noise level (feature 7 in Figure 6d). The seismic event marked as feature 8 in Figure 6c illustrates the importance of examining all potential parameters that might influence *dv*/*v*. Shortly, though not immediately, after the earthquake, we measure an abrupt velocity drop of almost 1% that, on first look, seems to be associated with the earthquake. However, the velocity decrease has a higher temporal correlation to the precipitation event occurring about 12 hr after the earthquake. Due to the high temporal resolution of the *dv*/*v* estimates, we can observe a few unaffected values after the earthquake and a rather sudden decrease coincident with the onset of a strong precipitation event. Therefore, we consider it the likelier cause for the observed velocity drop.

The largest seismic event during our study period is the M7.2 Zhupanov earthquake that struck on 30 January 2016 in the South of the peninsula about 250 km from Klyuchevskoy with a hypocentral depth of 177 km (see Figure 7). The earthquake-induced sudden velocity drops range between 0.1% and 0.5% across our network (Figure 6a feature 4 and Figures S13-S15 in Supporting Information S1). We determined the peak ground velocity (PGV) from the horizontal components of all active stations and show the result in Figure 7a. As expected, we find a higher PGV in the Central Kamchatka Depression (CKD) due to low shear wave velocities and its location closer to the epicenter (i.e., in the South). We then computed the ratio of the PGV and observed velocity drop, which we define as the difference between the average of the five data points (i.e., 12 hr) prior to and after the event's origin time, respectively (see Figure 7(b)). Most notably, station groups KVG and Shiveluch exhibit remarkably high $\frac{dv/v}{PGV}$ ratios, indicating a high sensitivity to the co-seismic shaking. These two station groups correspond to the stations located high up on the volcanic edifices of the Klyuchevskoy/Bezymianny massif and Shiveluch, respectively. ERidge, combining stations on the mountain range in the East, on the other hand, shows the lowest $\frac{dv/v}{PGV}$ ratios.

Previous studies have observed *dv*/*v* drops in volcanic areas that exceed these in neighboring areas by two or three times (Brenguier et al., 2014; Lesage et al., 2014). Lesage et al. (2014) observed a marked velocity drop at Volcán de Colima induced by the M7.4 Tecomán earthquake that struck about 140 km from the volcano. Regarding the magnitude and epicentral distance of the earthquake, their case is very similar to the one we observe in Kamchatka. They invoke material softening due to the pronounced non-linear elastic response of rocks with high porosity and pore space saturation - such as unconsolidated volcanic material (Johnson & Jia, 2005; Van Den Abeele, 2002). Brenguier et al. (2014) found that the M9.0 Tohoku-Oki earthquake induced higher velocity changes in active volcanic regions and ascribed this observation to the presence of pressurized fluids in the pore space amplifying the non-linear response even under increased confining pressure at depth.

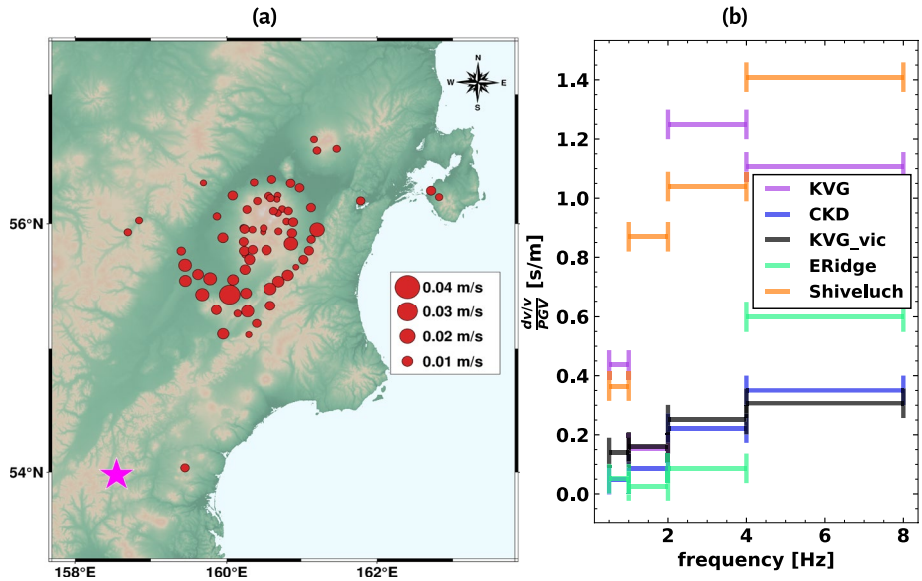

Figure 7. (a) Horizontal Peak ground velocities (PGVs) recorded during the M7.2 Zhupanov earthquake. The circles mark stations active on the day of the event, with their diameters scaling with PGV. We plot the epicenter of the Zhupanov earthquake as a star. (b) Corresponding $\frac{(dv/v)}{PGV}$ ratio for the different groups of stations and the examined frequency bands. The volcanic regions (Shiveluch and KVG) exhibit particularly high ratios.

For Kamchatka, tomography revealed high $\frac{v_P}{v_S}$ ratios in shallow regions below the KVG, indicating a high water content in sediments of the CKD and in the volcanic edifices (Green et al., 2020; Ivanov et al., 2016; Koulakov et al., 2017, 2021). Also, the presence of hydrothermal reservoirs is well documented (e.g., Kiryukhin et al., 2012; Taran, 2009), for which a higher sensitivity to ground shaking was observed (e.g., Caudron et al., 2022; Chaves & Schwartz, 2016; Taira & Brenguier, 2016). However, Shiveluch is not equally well studied and only a few images exist that, contrary to the implication of the higher $\frac{dv/v}{PGV}$ ratio at the highest frequencies, show a high $\frac{v_P}{v_S}$ zone that is slightly deeper than the one under the KVG (Koulakov, 2021; Koulakov et al., 2020). This could either be an indication that additional seismic data around Shiveluch are required to improve our understanding of the crustal structure below Shiveluch or simply be within the uncertainty of our data - particularly around Shiveluch, where the station coverage is lower.

Generally, the non-linear stress-strain behavior of rocks appears to depend on material inhomogeneities, such as pores, cracks, or matrix/clast distribution that lead to the formation of force chains and a concentration of stress at "stability bridges" in the material (Sens-Schönfelder et al., 2019). Volcanic rocks are highly heterogeneous (Schaefer et al., 2015), therefore, we expect a significant contribution of non-linear elasticity to the observed *dv*/*v* response. However, based on this discussion, we suspect that both elastic non-linearity and the presence of fluids in the pore space contribute to the pronounced velocity reduction at the KVG and Shiveluch. We expect that the magnitude of the contribution of each of these factors depends on the pore space saturation (or pressurization) at the time of shaking. In practice, that could mean that volcanoes with higher pressurization are more susceptible to ground shaking (as proposed by Brenguier et al., 2014). In the present case, we neither observe nor expect significant differences in pressurization between Shiveluch, Klyuchevskoy, and Bezymianny because they are fed by the same magma system (e.g., Koulakov, 2021) and had recent eruptions (i.e., <10 years before the data collection).

5.3. Influence of Volcanic Activity

A previous study by Coppola et al. (2021) has revealed a complex relationship between the major volcanoes of the KVG and a potential modulation by tectonic triggers. At Klyuchevskoy and Bezymianny, a period of unrest commenced in 2016, accompanied by eruptive activity (Journeau et al., 2022; Mania et al., 2019, 2021). For Bezymianny Volcano, Mania et al. (2019) found signs of an extrusion onset in early 2016, which is why we focus on stations in Bezymianny's vicinity. Unfortunately, stations D0.BZM, D0.BZW, X9.B07, X9.B08, X9.SV8, and X9.SV9 on the volcanic edifice failed in late 2015 and early 2016 leading to a lower spatial sensitivity, but

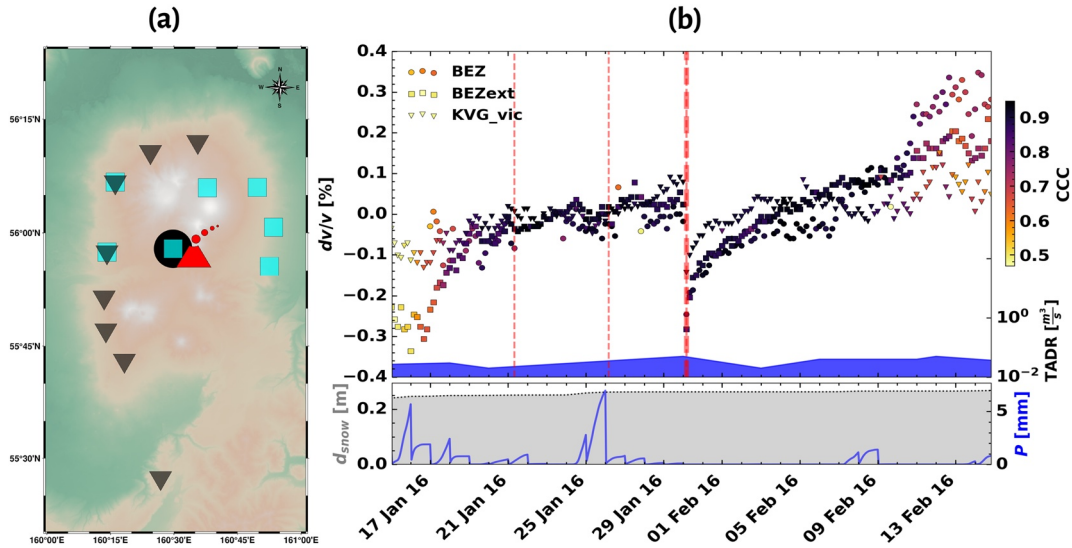

Figure 8. (a) Definition of the station groupings used in (b). (b) Evolution of the seismic velocity as computed from auto and self-correlations between 15 January 2016 and 15 February 2016 close to Bezymianny Volcano at 2–4 Hz. We show *dv/v* estimates as colored symbols (matched with symbols in (a)) with color scaling dependent upon the cumulative correlation coefficient. Each point represents a time window of 2 hrs. Red vertical dashed lines mark the origin times of regional earthquakes with a magnitude ≥4.8. The bold dashed line marks the 30 January 2016 M7.2 Zhupanov earthquake. The time-averaged lava discharge rate (TADR) of Bezymianny is plotted logarithmically in blue. In the lower panel, we show precipitation and snow load data in water equivalent averaged over all locations of the station group KVG_vic. Toward the end of the time window, we measure an especially strong increase in the seismic velocity at station D0.BZG (circles). Simultaneously, we see a decorrelation at all shown groups.

permanent station D0.BZG near the summit was fortunately operational throughout this episode and delivers stable *dv/v* estimates.

Satellite synthetic aperture RADAR (SAR) offset tracking reveals the first evidence of a starting plug extrusion at Bezymianny between January and April 2016 (see Figure S9 in Supporting Information S1, and Mania et al., 2019). With an intermittent uplift but almost continuously increasing uplift rate, the average crater offset reached about 1.5 m on 16 February 2016. With 4 hr, the *dv/v* time series presented in Figure 8 affords a significantly higher time resolution than the SAR data provided in Figure S9 in Supporting Information S1, which has a maximum resolution of 11 days. From the *dv/v* time series, we estimate a gradual velocity increase of about 0.3% at D0.BZG initiating around 6-7 February, which we interpret as an expression of deeper medium changes associated with the surface deformation estimated by pixel offset. In conjunction with the velocity increase at BZG, we find a decorrelation (i.e., a decreasing CCC) at several stations surrounding Bezymianny (see Figure 8). The velocity increase at BZG exceeds the effects of snow compaction and damage recovery observed at all the other stations and is significant with respect to the short-term fluctuations.

Many studies linked volcanic inflation to *dv/v* decreases rather than increases (e.g., Brenguier et al., 2011; Brenguier et al., 2016; De Plaen et al., 2016, 2019; Machacca-Puma et al., 2019; Takano et al., 2017). However, local velocity increases could occur if a shallow magma, gas, or hydrothermal reservoir, as it may exist beneath Bezymianny (Ivanov et al., 2016; Koulakov et al., 2017, 2021), inflates and, thereby, causes local compaction through increased pressure (Caudron et al., 2021, 2022; Donaldson et al., 2017, 2019; Hotovec-Ellis et al., 2015; Yates et al., 2019). Our hypothesis is further supported by a recently published study by Berezhnev et al. (2023), who found increasing velocities at Bezymianny immediately before its 2017 eruption. They modeled the mechanical deformation associated with the observed velocity changes and concluded that an inflating shallow reservoir is the most likely cause for the changing velocity.

A combination of localized velocity increases and decreases in the vicinity of Bezymianny, as expected to arise from a shallow pressure source (Donaldson et al., 2017), would also lead to decreasing correlation. As with any inhomogeneous velocity change, these decreases and increases would cause the shapes of the CFs to alter significantly, resulting in a decorrelation. Alternatively, the observed decorrelation could have resulted from other

modulations of the scattering properties of the subsurface due to incipient deformation of the volcanic edifice (Obermann, Planès, Larose, & Campillo, 2013).

The closely spaced occurrences of the Zhupanov earthquake, the detected velocity increase at BZG, and the proposed initiation of Bezymianny's eruptive cycle (Mania et al., 2019) are noteworthy. It raises the question of whether Bezymianny's 2016/2017 eruption was tectonically triggered as reported in some rare cases (Hill et al., 2002; Kennedy, 2017; Seropian et al., 2021; Walter & Amelung, 2007; Watt et al., 2009). However, based on the currently available data, we would consider such conclusions speculative.

6. Conclusions

6.1. Time-Segmented Passive Image Interferometry for Fluctuant Noise Fields

For data from KVG, established preprocessing strategies and PII algorithms were not sufficient to produce stable velocity change estimates for high frequencies (>∼ 1 Hz) and fine temporal resolutions (<∼1 week) as needed to understand the effect of several forcing mechanisms operating at these and lower time scales. In this paper, we demonstrate that PII is feasible even in the presence of pronounced, long-lasting fluctuations of the noise wavefield if one applies the *time-segmented passive image interferometry* (TSPII) technique, as proposed here. We utilize a hierarchical clustering algorithm to find time windows with temporarily stationary noise fields suitable for separate PII surveys. Subsequently, we spatially average the results to increase the temporal resolution even further.

In its current form, TSPII is best suited for settings where the noise field has several distinct "modes", for example, spatially stable noise sources, which stay active or inactive over extended periods. Therefore, it is particularly well-suited for volcanic environments with long-lasting phases of tremor activity. In cases with sporadic, rapid shifts, approaches based on filters are more likely to be successful.

6.2. Evolution of the Seismic Velocity at the Klyuchevskoy Volcano Group

After applying TSPII and spatial averaging, we present velocity change observations for Kamchatka from five different regions for five-time segments and various frequency bands. When analyzing the velocity changes, we find dominant forcing from environmental factors. We analyze dv/v time series computed from high-frequency data (>2 Hz), which exhibits a lower noise level and a higher resolution than the time series from lower frequencies (<1 Hz). High frequencies are particularly sensitive to pore pressure changes in the shallow subsurface. The pore pressure, in turn, is strongly impacted by precipitation leading to immediate short-term velocity decreases following precipitation events. In contrast, increasing snow depth causes a velocity increase. These findings again emphasize the value of PII in monitoring the vadose zone, which is a vital component for groundwater recharge and drainage cycles. Monitoring groundwater levels is especially critical in regions with little precipitation or strongly pronounced dry seasons. To these ends, PII provides a low-cost, non-invasive method that probes the vicinity of the station rather than only a single spot as a well would. We present a simple model that relates snow load and precipitation to the seismic velocity reproducing first-order variations in dv/v.

In addition to environmental events, we find impacts of tectonic events - first and foremost, the M7.2 Zhupanov earthquake, which leads to high-amplitude damage-induced velocity drops across the network with subsequent recovery. The amplitude of said velocity drop is not solely dependent on the strength of the ground shaking, which we quantify by computing the peak ground velocity. Instead, we find that volcanic regions (i.e., the KVG and Shiveluch) are more sensitive to ground shaking and experience more pronounced velocity drops. For Kamchatka, we explain this unusually high dv/v response with the non-classical non-linear behavior of the volcanic rock, possibly amplified by the high fluid contents in the pore space.

Lastly, we see a marked velocity increase accompanied by a decorrelation of the noise correlation functions at Bezymianny Volcano commencing 6–7 February 2016, shortly after the Zhupanov earthquake. The velocity increase occurs together with a first uplift marking the beginning of the 2016/2017 eruption cycle (Coppola et al., 2021; Mania et al., 2019, 2021). We argue that the inflation of a shallow gas, magma, or hydrothermal reservoir could cause localized velocity increases and decreases. This inhomogeneous velocity change combined with the deformation of the volcanic edifice would lead to the observed apparent homogeneous velocity change close to the deformation and a net-zero velocity change in the far-field, concurrently inducing the decorrelation at

all locations. Our study, once again, demonstrates that passive image interferometry is a valuable tool for monitoring volcanic deformation, possibly in near real-time and with a denser temporal sampling than, for example, satellite-based techniques could resolve.

Data Availability Statement

The KISS dataset (Shapiro et al., 2015, https://doi.org/10.14470/K47560642124) is openly available via the GFZ Data Services. Access to the data recorded by the D0 seismic network is restricted but can be obtained via the GFZ Data Services. The ERA5 climate data (Muñoz Sabater, 2019, doi: https://doi.org/10.24381/cds.e2161bac) are available upon registration at https://cds.climate.copernicus.eu/cdsapp#!/dataset/10.24381/cds.e2161bac?tab=overview. The TADR datasets are provided as supplementary material to Coppola et al. (2021). All TerraSAR-X data are available through the German Aerospace Centre (DLR). The origin times of the seismic events plotted in Sections 4 and 5 can be queried via the USGS FDSN web service. The seismic data download and the computation of correlations and *dv/v* were executed using SeisMIC 0.1.28 (Makus & Sens-Schönfelder, 2022, doi: https://doi.org/10.5880/GFZ.2.4.2022.002), available under the EUPL license agreement at https://github.com/PeterMakus/SeisMIC. TheSequencer algorithm (Baron & Ménard, 2021) that we used to sort the similarity matrices of the stations can be executed online at http://sequencer.org, its source code can be downloaded at https://github.com/dalya/Sequencer. TheSequencer is licensed under the MIT license agreement. All maps were plotted using PyGMT (Uieda et al., 2022, doi: https://doi.org/10.5281/zenodo.7481934). For Figures 1a, 4, and 7a, we used the SRTM15+ digital elevation model (DEM) by Tozer et al. (2019). For Figures 1b and 8a, we obtained the SRTMGL1 DEM from NASAJPL (2013).

Acknowledgments
We are grateful for the discussions with Marine Denolle that helped to improve this manuscript. We also thank Diego Coppola for providing the TADR datasets of Bezymianny and Klyuchevskoy. We thank Nikolai Shapiro, Ivan Koulakov, and the many other colleagues who were involved in the KISS temporary deployment as well as the GFZ GIPP pool for providing the corresponding stations, and the Kamchatka Branch of Geophysical Survey of the Russian Academy of Sciences for collecting the seismic data of the D0 network and making it available. We thank the DLR for their support; the acquisition of the spot-mode TerraSAR-X data was realized through proposal GEO1505 to Thomas R. Walter. This work was supported by the DFG grant SE1844/12-1. We thank Dr Corentin Caudron and one anonymous reviewer for their valuable comments that helped to improve this manuscript. Open Access funding enabled and organized by Projekt DEAL.

References

Andajani, R. D., Tsuji, T., Snieder, R., & Ikeda, T. (2020). Spatial and temporal influence of rainfall on crustal pore pressure based on seismic velocity monitoring. *Earth Planets and Space*, *72*(1), 1–17. https://doi.org/10.1186/s40623-020-01311-1

Baron, D., & Ménard, B. (2021). Extracting the main trend in a data set: The sequencer algorithm. *The Astrophysical Journal*, *916*(2), 91. https://doi.org/10.3847/1538-4357/abfc4d

Belousov, A., Voight, B., Belousova, M., & Muravyev, Y. (2000). Tsunamis generated by subaquatic volcanic explosions: Unique data from 1996 eruption in Karymskoye lake, kamchatka, Russia. *Pure and Applied Geophysics*, *157*(6–8), 1135–1143. https://doi.org/10.1007/s000240050021

Bennington, N. L., Haney, M., De Angelis, S., Thurber, C. H., & Freymueller, J. (2015). Monitoring changes in seismic velocity related to an ongoing rapid inflation event at Okmok volcano, Alaska. *Journal of Geophysical Research: Solid Earth*, *120*(8), 5664–5676. https://doi.org/10.1002/2015JB011939

Berezhnev, Y., Belovezhets, N., Shapiro, N., & Koulakov, I. (2023). Temporal changes of seismic velocities below bezymianny volcano prior to its explosive eruption on 20.12. 2017. *Journal of Volcanology and Geothermal Research*, *433*, 107735. https://doi.org/10.1016/j.jvolgeores.2022.107735

Bonilla, L. F., Guéguen, P., & Ben-Zion, Y. (2019). Monitoring seismic temporal changes of shallow material during strong ground motion with interferometry and autocorrelation. *Bulletin of the Seismological Society of America*, *109*(1), 187–198. https://doi.org/10.1785/0120180092

Boschelli, J., Moschetti, M. P., & Sens-Schönfelder, C. (2021). Temporal seismic velocity variations: Recovery following from the 2019 M w 7.1 Ridgecrest, California earthquake. *Journal of Geophysical Research: Solid Earth*, *126*(4). https://doi.org/10.1029/2020jb021465

Brenguier, F., Campillo, M., Hadziioannou, C., Shapiro, N. M., Nadeau, R. M., & Larose, E. (2008a). Postseismic Relaxation along the san Andreas fault at Parkfield from continuous Seismological observations. *Science*, *321*(5895), 1478–1481. https://doi.org/10.1126/science.1160943

Brenguier, F., Campillo, M., Takeda, T., Aoki, Y., Shapiro, N. M., Briand, X., et al. (2014). Mapping pressurized volcanic fluids from induced crustal seismic velocity drops. *Science*, *345*(6192), 80–82. https://doi.org/10.1126/science.1254073

Brenguier, F., Clarke, D., Aoki, Y., Shapiro, N. M., Campillo, M., & Ferrazzini, V. (2011). Monitoring volcanoes using seismic noise correlations. *Comptes Rendus Geoscience*, *343*(8–9), 633–638. https://doi.org/10.1016/j.crte.2010.12.010

Brenguier, F., Rivet, D., Obermann, A., Nakata, N., Boué, P., Lecocq, T., et al. (2016). 4-D noise-based seismology at volcanoes: Ongoing efforts and perspectives. *Journal of Volcanology and Geothermal Research*, *321*, 182–195. https://doi.org/10.1016/j.jvolgeores.2016.04.036

Brenguier, F., Shapiro, N. M., Campillo, M., Ferrazzini, V., Duputel, Z., Coutant, O., & Nercessian, A. (2008b). Towards forecasting volcanic eruptions using seismic noise. *Nature Geoscience*, *1*(2), 126–130. https://doi.org/10.1038/ngeo104

Budi-Santoso, A., Lesage, P., Dwiyono, S., Sumarti, S., Subandriyo, S., Surono, et al. (2013). Analysis of the seismic activity associated with the 2010 eruption of Merapi Volcano, Java. *Journal of Volcanology and Geothermal Research*, *261*(November 2010), 153–170. https://doi.org/10.1016/j.jvolgeores.2013.03.024

Bürgmann, R., Kogan, M. G., Steblov, G. M., Hilley, G., Levin, V. E., & Apel, E. (2005). Interseismic coupling and asperity distribution along the Kamchatka subduction zone. *Journal of Geophysical Research*, *110*(7), 1–17. https://doi.org/10.1029/2005JB003648

Caudron, C., Aoki, Y., Lecocq, T., De Plaen, R., Soubestre, J., Mordret, A., et al. (2022). Hidden pressurized fluids prior to the 2014 phreatic eruption at mt ontake. *Nature Communications*, *13*(1), 1–9. https://doi.org/10.1038/s41467-022-32252-w

Caudron, C., Girona, T., Jolly, A., Christenson, B., Savage, M. K., Carniel, R., et al., others (2021). A quest for unrest in multiparameter observations at whakaari/white island volcano, New Zealand 2007–2018. *Earth Planets and Space*, *73*(1), 1–21. https://doi.org/10.1186/s40623-021-01506-0

Chaves, E. J., & Schwartz, S. Y. (2016). Monitoring transient changes within overpressured regions of subduction zones using ambient seismic noise. *Science Advances*, *2*(1), 1–7. https://doi.org/10.1126/sciadv.1501289

Chouet, B. A. (1996). Long-period volcano seismicity: Its source and use in eruption forecasting. *Nature*, *380*(6572), 309–316. https://doi.org/10.1038/380309a0

Clements, T., & Denolle, M. A. (2018). Tracking groundwater levels using the ambient seismic field. *Geophysical Research Letters*, *45*(13), 6459–6465. https://doi.org/10.1029/2018GL077706

Coppola, D., Marco, L., Massimetti, F., Hainzl, S., Shevchenko, A. V., Mania, R., et al. (2021). Thermal remote sensing reveals communication between volcanoes of the Klyuchevskoy Volcanic Group. *Scientific Reports*, *11*(1), 1–16. https://doi.org/10.1038/s41598-021-92542-z

De Plaen, R. S., Cannata, A., Cannavo', F., Caudron, C., Lecocq, T., & Francis, O. (2019). Temporal changes of seismic velocity caused by volcanic activity at Mt. Etna revealed by the autocorrelation of ambient seismic noise. *Frontiers of Earth Science*, *6*(January), 1–11. https://doi.org/10.3389/feart.2018.00251

De Plaen, R. S., Lecocq, T., Caudron, C., Ferrazzini, V., & Francis, O. (2016). Single-station monitoring of volcanoes using seismic ambient noise. *Geophysical Research Letters*, *43*(16), 8511–8518. https://doi.org/10.1002/2016GL070078

Donaldson, C., Caudron, C., Green, R. G., Thelen, W. A., & White, R. S. (2017). Relative seismic velocity variations correlate with deformation at Kīlauea volcano. *Science Advances*, *3*(6), 1–12. https://doi.org/10.1126/sciadv.1700219

Donaldson, C., Winder, T., Caudron, C., & White, R. S. (2019). Crustal seismic velocity responds to a magmatic intrusion and seasonal loading in Iceland's Northern Volcanic Zone. *Science Advances*, *5*(11). https://doi.org/10.1126/sciadv.aax6642

Dorendorf, F., Wiechert, U., & Wörner, G. (2000). Hydrated sub-are mantle: A source for the Kluchevskoy volcano, kamchatka/Russia. *Earth and Planetary Science Letters*, *175*(1–2), 69–86. https://doi.org/10.1016/s0012-821x(99)00288-5

Droznin, D. V., Shapiro, N. M., Droznina, S. Y., Senyukov, S. L., Chebrov, V. N., & Gordeev, E. I. (2015). Detecting and locating volcanic tremors on the Klyuchevskoy group of volcanoes (Kamchatka) based on correlations of continuous seismic records. *Geophysical Journal International*, *203*(2), 1001–1010. https://doi.org/10.1093/gji/ggv342

Fedotov, S. A., Zharinov, N. A., & Gontovaya, L. I. (2010). The magmatic system of the Klyuchevskaya group of volcanoes inferred from data on its eruptions, earthquakes, deformation, and deep structure. *Journal of Volcanology and Seismology*, *4*(1), 1–33. https://doi.org/10.1134/S074204631001001X

Feng, K.-F., Huang, H.-H., Hsu, Y.-J., & Wu, Y.-M. (2021). Controls on seasonal variations of crustal seismic velocity in taiwan using single-station cross-component analysis of ambient noise interferometry. *Journal of Geophysical Research: Solid Earth*, *126*(11), e2021JB022650. https://doi.org/10.1029/2021JB022650

Fichtner, A., & Tsai, V. C. (2019). Theoretical Foundations of noise interferometry. In *Seismic ambient noise* (pp. 109–143). Cambridge University Press. https://doi.org/10.1017/9781108264808.006

Fontaine, F. R., Roult, G., Michon, L., Barruol, G., & Muro, A. D. (2014). The 2007 eruptions and caldera collapse of the Piton de la Fournaise volcano (La Réunion Island) from tilt analysis at a single very broadband seismic station. *Geophysical Research Letters*, *41*(8), 2803–2811. https://doi.org/10.1002/2014GL059691

Gassenmeier, M., Sens-Schönfelder, C., Delatre, M., & Korn, M. (2014). Monitoring of environmental influences on seismic velocity at the geological storage site for CO2 in Ketzin (Germany) with ambient seismic noise. *Geophysical Journal International*, *200*(1), 524–533. https://doi.org/10.1093/gji/ggu413

Girina, O. A., Manevich, A. G., Melnikov, D. V., Nuzhdaev, A. A., & Petrova, E. G. (2019). The 2016 eruptions in kamchatka and on the north Kuril Islands: The Hazard to aviation. *Journal of Volcanology and Seismology*, *13*(3), 157–171. https://doi.org/10.1134/S0742046319030047

Gómez-García, C., Brenguier, F., Boué, P., Shapiro, N. M., Droznin, D. V., Droznina, S. Y., et al. (2018). Retrieving robust noise-based seismic velocity changes from sparse data sets: Synthetic tests and application to klyuchevskoy volcanic group (kamchatka). *Geophysical Journal International*, 1218–1236. https://doi.org/10.1093/gji/ggy190

Green, R. G., Sens-Schönfelder, C., Shapiro, N., Koulakov, I., Tilmann, F., Dreiling, J., et al. (2020). Magmatic and sedimentary structure beneath the klyuchevskoy volcanic group, kamchatka, from ambient noise tomography. *Journal of Geophysical Research: Solid Earth*, *125*(3). https://doi.org/10.1029/2019JB018900

Guillemot, A., Van Herwijnen, A., Larose, E., Mayer, S., & Baillet, L. (2021). Effect of snowfall on changes in relative seismic velocity measured by ambient noise correlation. *The Cryosphere*, *15*(12), 5805–5817. https://doi.org/10.5194/tc-15-5805-2021

Hadziioannou, C., Larose, E., Baig, A., Roux, P., & Campillo, M. (2011). Improving temporal resolution in ambient noise monitoring of seismic wave speed. *Journal of Geophysical Research*, *116*(7), 1–10. https://doi.org/10.1029/2011JB008200

Heki, K. (2001). Seasonal modulation of interseismic strain buildup in northeastern Japan driven by snow loads. *Science*, *293*(5527), 89–92. https://doi.org/10.1126/science.1061056

Hersbach, H., Bell, B., Berrisford, P., Hirahara, S., Horányi, A., Muñoz-Sabater, J., et al. (2020). The ERA5 global reanalysis. *Quarterly Journal of the Royal Meteorological Society*, *146*(730), 1999–2049. https://doi.org/10.1002/qj.3803

Hillers, G., Ben-Zion, Y., Campillo, M., & Zigone, D. (2015). Seasonal variations of seismic velocities in the San Jacinto fault area observed with ambient seismic noise. *Geophysical Journal International*, *202*(2), 920–932. https://doi.org/10.1093/gji/ggv151

Hillers, G., Campillo, M., & Ma, K. F. (2014). Seismic velocity variations at TCDP are controlled by MJO driven precipitation pattern and high fluid discharge properties. *Earth and Planetary Science Letters*, *391*, 121–127. https://doi.org/10.1016/j.epsl.2014.01.040

Hill, D. P., Pollitz, F., & Newhall, C. (2002). Earthquake-Volcano Interactions. New measurements, statistical analyses, and models support can trigger subsequent long distance times scales. *Physics Today*, *55*(11), 41–47. https://doi.org/10.1063/1.1535006

Hirose, T., Nakahara, H., & Nishimura, T. (2017). Combined use of repeated active shots and ambient noise to detect temporal changes in seismic velocity: Application to Sakurajima volcano, Japan 4. Seismology. *Earth Planets and Space*, *69*(1), 42. https://doi.org/10.1186/s40623-017-0613-7

Hobiger, M., Wegler, U., Shiomi, K., & Nakahara, H. (2014). Single-station cross-correlation analysis of ambient seismic noise: Application to stations in the surroundings of the 2008 Iwate-Miyagi Nairiku earthquake. *Geophysical Journal International*, *198*(1), 90–109. https://doi.org/10.1093/gji/ggu115

Hobiger, M., Wegler, U., Shiomi, K., & Nakahara, H. (2016). Coseismic and post-seismic velocity changes detected by passive image interferometry: Comparison of one great and five strong earthquakes in Japan. *Geophysical Journal International*, *205*(2), 1053–1073. https://doi.org/10.1093/gji/ggw066

Hotovec-Ellis, A. J., Gomberg, J., Vidale, J., & Creager, K. C. (2014). A continuous record of interruption velocity change at mount st. Helens from coda wave interferometry. *Journal of Geophysical Research: Solid Earth*, *119*(3), 2199–2214. https://doi.org/10.1002/2013JB010742

Hotovec-Ellis, A. J., Vidale, J. E., Gomberg, J., Thelen, W., & Moran, S. C. (2015). Changes in seismic velocity during the first 14 months of the 2004-2008 eruption of Mount St. Helens, Washington. *Journal of Geophysical Research: Solid Earth*, *120*(9), 6226–6240. https://doi.org/10.1002/2015JB012101

Illien, L., Andermann, C., Sens-Schönfelder, C., Cook, K. L., Baidya, K. P., Adhikari, L. B., & Hovius, N. (2021). Subsurface moisture regulates Himalayan groundwater storage and discharge. *AGU Advances*, *2*(2). https://doi.org/10.1029/2021av000398

Illien, L., Sens-Schönfelder, C., & Ke, K.-Y. (2023). Resolving minute temporal seismic velocity changes induced by earthquake damage: The more stations, the merrier. *Geophysical Journal International*, *234*(1), ggad038-135. https://doi.org/10.1093/gji/ggad038

Ivanov, A. I., Koulakov, I. Y., West, M., Jakovlev, A. V., Gordeev, E. I., Senyukov, S., & Chebrov, V. N. (2016). Magma source beneath the Bezymianny volcano and its interconnection with Klyuchevskoy inferred from local earthquake seismic tomography. *Journal of Volcanology and Geothermal Research*, *323*, 62–71. https://doi.org/10.1016/j.jvolgeores.2016.04.010

James, S. R., Knox, H. A., Abbott, R. E., Panning, M. P., & Screaton, E. J. (2019). Insights into permafrost and seasonal active-layer dynamics from ambient seismic noise monitoring. *Journal of Geophysical Research: Earth Surface*, *124*(7), 1798–1816. https://doi.org/10.1029/2019JF005051

Johnson, P. A., & Jia, X. (2005). Nonlinear dynamics, granular media and dynamic earthquake triggering. *Nature*, *437*(7060), 871–874. https://doi.org/10.1038/nature04015

Journeau, C., Shapiro, N. M., Seydoux, L., Soubestre, J., Koulakov, I. Y., Jakovlev, A. V., et al. (2022). Seismic tremor reveals active trans-crustal magmatic system beneath Kamchatka volcanoes. *Science Advances*, *8*(5), 1–12. https://doi.org/10.1126/sciadv.abj1571

Kayzar, T. M., Nelson, B. K., Bachmann, O., Bauer, A. M., & Izbekov, P. E. (2014). Deciphering petrogenic processes using Pb isotope ratios from time-series samples at Bezymianny and Klyuchevskoy volcanoes, Central Kamchatka Depression. *Contributions to Mineralogy and Petrology*, *168*(4), 1–28. https://doi.org/10.1007/s00410-014-1067-6

Kennedy, B. (2017). What effects do earthquakes have on volcanoes? *Geology*, *45*(8), 765–766. https://doi.org/10.1130/focus0820172.1

Kiryukhin, A. V., Rychkova, T. V., & Dubrovskaya, I. K. (2012). formation of the hydrothermal system in Geysers valley (Kronotsky nature Reserve, kamchatka) and triggers of the giant Landslide. *Applied Geochemistry*, *27*(9), 1753–1766. https://doi.org/10.1016/j.apgeochem.2012.02.011

Koulakov, I. (2021). Seismic tomography of Kamchatkan volcanoes. *Russian Geology and Geophysics*, *1815*(11), 1–38. https://doi.org/10.2113/rgg20214380

Koulakov, I., Abkadyrov, I., Al Arifi, N., Deev, E., Droznina, S., Gordeev, E. I., et al. (2017). Three different types of plumbing system beneath the neighboring active volcanoes of Tolbachik, Bezymianny, and Klyuchevskoy in Kamchatka. *Journal of Geophysical Research: Solid Earth*, *122*(5), 3852–3874. https://doi.org/10.1002/2017JB014082

Koulakov, I., Gordeev, E. I., Dobretsov, N. L., Vernikovsky, V. A., Senyukov, S., Jakovlev, A., & Jaxybulatov, K. (2013). Rapid changes in magma storage beneath the Klyuchevskoy group of volcanoes inferred from time-dependent seismic tomography. *Journal of Volcanology and Geothermal Research*, *263*, 75–91. https://doi.org/10.1016/j.jvolgeores.2012.10.014

Koulakov, I., Plechov, P., Mania, R., Walter, T. R., Smirnov, S. Z., Abkadyrov, I., et al. (2021). Anatomy of the Bezymianny volcano merely before an explosive eruption on 20.12.2017. *Scientific Reports*, *11*(1), 1–12. https://doi.org/10.1038/s41598-021-81498-9

Koulakov, I., Shapiro, N. M., Sens-Schönfelder, C., Luehr, B. G., Gordeev, E. I., Jakovlev, A., et al. (2020). Mantle and crustal sources of magmatic activity of klyuchevskoy and surrounding volcanoes in kamchatka inferred from earthquake tomography. *Journal of Geophysical Research: Solid Earth*, *125*(10), e2020JB020097. https://doi.org/10.1029/2020JB020097

Lesage, P., Reyes-Dávila, G., & Arámbula-Mendoza, R. (2014). Large tectonic earthquakes induce sharp temporary decreases in seismic velocity in Volcán de Colima, Mexico. *Journal of Geophysical Research: Solid Earth*, *119*(5), 4360–4376. https://doi.org/10.1002/2013JB010884

Lindner, F., Wassermann, J., & Igel, H. (2021). Seasonal freeze-thaw cycles and permafrost degradation on Mt. Zugspitze (German/Austrian Alps) revealed by single-station seismic monitoring. *Geophysical Research Letters*, *48*(18), 1–11. https://doi.org/10.1029/2021GL094659

Machacca-Puma, R., Lesage, P., Larose, E., Lacroix, P., & Anccasi-Figueroa, R. M. (2019). Detection of pre-eruptive seismic velocity variations at an andesitic volcano using ambient noise correlation on 3-component stations: Ubinas volcano, Peru, 2014. *Journal of Volcanology and Geothermal Research*, *381*, 83–100. https://doi.org/10.1016/j.jvolgeores.2019.05.014

Makus, P., & Sens-Schönfelder, C. (2022). Seismological monitoring using interferometric Concepts (SeisMIC) [Software]. GFZ Data Services. https://doi.org/10.5880/GFZ.2.4.2022.002

Mania, R., Cesca, S., Walter, T. R., Koulakov, I., & Senyukov, S. L. (2021). Inflating shallow plumbing system of Bezymianny Volcano, kamchatka, studied by InSAR and seismicity data prior to the 20 December 2017 eruption. *Frontiers of Earth Science*, *9*(December), 1–17. https://doi.org/10.3389/feart.2021.765668

Mania, R., Walter, T. R., Belousova, M., Belousov, A., & Senyukov, S. L. (2019). Deformations and morphology changes associated with the 2016-2017 eruption sequence at Bezymianny volcano, Kamchatka. *Remote Sensing*, *11*(11), 1278. https://doi.org/10.3390/rs11111278

Mao, S., Lecointre, A., van der Hilst, R. D., & Campillo, M. (2022). Space-time monitoring of groundwater fluctuations with passive seismic interferometry. *Nature Communications*, *13*(1), 1–9. https://doi.org/10.1038/s41467-022-32194-3

Massonnet, D., Briole, P., & Arnaud, A. (1995). Deflation of Mount Etna monitored by spaceborne radar interferometry. *Nature*, *375*(6532), 567–570. https://doi.org/10.1038/375567a0

Mordret, A., Mikesell, T. D., Harig, C., Lipovsky, B. P., & Prieto, G. A. (2016). Monitoring southwest Greenland's ice sheet melt with ambient seismic noise. *Science Advances*, *2*(5), e1501538. https://doi.org/10.1126/sciadv.1501538

Moreau, L., Stehly, L., Boué, P., Lu, Y., Larose, E., & Campillo, M. (2017). Improving ambient noise correlation functions with an SVD-based Wiener filter. *Geophysical Journal International*, *211*(1), 418–426. https://doi.org/10.1093/GJI/GGX306

Müllner, D. (2013). Fastcluster: Fast hierarchical, agglomerative clustering routines for R and Python. *Journal of Statistical Software*, *53*(9), 1–18. https://doi.org/10.18637/jss.v053.i09

Muñoz Sabater, J. (2019). Era5-land hourly data from 1981 to present) [Dataset]. Copernicus Climate Change Service (C3S) Climate Data Store (CDS). https://doi.org/10.24381/cds.e2161bac

NASAJPL. (2013). Nasa shuttle radar topography mission global 1 arc second) [Dataset]. NASA EOSDIS Land Processes DAAC. https://doi.org/10.5067/MEaSUREs/SRTM/SRTMGL1.003

Obermann, A., Planes, T., Hadziioannou, C., & Campillo, M. (2016). Lapse-time-dependent coda-wave depth sensitivity to local velocity perturbations in 3-d heterogeneous elastic media. *Geophysical Journal International*, *207*(1), 59–66. https://doi.org/10.1093/gji/ggw264

Obermann, A., Planès, T., Larose, E., & Campillo, M. (2013). Imaging preeruptive and coeruptive structural and mechanical changes of a volcano with ambient seismic noise. *Journal of Geophysical Research: Solid Earth*, *118*(12), 6285–6294. https://doi.org/10.1002/2013JB010399

Obermann, A., Planès, T., Larose, E., Sens-Schönfelder, C., & Campillo, M. (2013). Depth sensitivity of seismic coda waves to velocity perturbations in an elastic heterogeneous medium. *Geophysical Journal International*, *194*(1), 372–382. https://doi.org/10.1093/gji/ggt043

Olivier, G., Brenguier, F., Carey, R., Okubo, P., & Donaldson, C. (2019). Decrease in seismic velocity observed prior to the 2018 eruption of Kīlauea volcano with ambient seismic noise interferometry. *Geophysical Research Letters*, *46*(7), 3734–3744. https://doi.org/10.1029/2018GL081609

Ozerov, A. Y., Ariskin, A. A., Kyle, P., Bogoyavlenskaya, G. E., & Karpenko, S. F. (1997). Petrological-geochemical model for genetic relationships between basaltic and andesitic magmatism of Klyuchevskoi and Bezymyannyi volcanoes, Kamchatka. *Petrology*, *5*(6), 550–569.

Peltier, A., Ferrazzini, V., Staudacher, T., & Bachèlery, P. (2005). Imaging the dynamics of dyke propagation prior to the 2000-2003 flank eruptions at Piton de la Fournaise, Reunion Island. *Geophysical Research Letters*, *32*(22), 1–5. https://doi.org/10.1029/2005GL023720

Ratdomopurbo, A., & Poupinet, G. (1995). Monitoring a temporal change of seismic velocity in a volcano: Application to the 1992 eruption of Mt. Merapi (Indonesia). *Geophysical Research Letters*, *22*(7), 775–778. https://doi.org/10.1029/95GL00302

Rodríguez Tribaldos, V., & Ajo-Franklin, J. B. (2021). Aquifer monitoring using ambient seismic noise recorded with distributed acoustic sensing (DAS) deployed on dark fiber. *Journal of Geophysical Research: Solid Earth*, *126*(4), 1–20. https://doi.org/10.1029/2020JB021004

Ruiz, M. Z., Civilini, F., Ebinger, C. J., Oliva, S. J., Ruiz, M. C., Badi, G., et al. (2022). Precursory signal detected for the 2018 Sierra Negra volcanic eruption, Galápagos, using seismic ambient noise. *Journal of Geophysical Research: Solid Earth*, *127*(3), 1–16. https://doi.org/10.1029/2021jb022990

Schaefer, L. N., Kendrick, J. E., Oommen, T., Lavallée, Y., & Chigna, G. (2015). Geomechanical rock properties of a basaltic volcano. *Frontiers of Earth Science*, *3*(June), 1–15. https://doi.org/10.3389/feart.2015.00029

Schimmel, M., Stutzmann, E., & Gallart, J. (2011). Using instantaneous phase coherence for signal extraction from ambient noise data at a local to a global scale. *Geophysical Journal International*, *184*(1), 494–506. https://doi.org/10.1111/j.1365-246X.2010.04861.x

Sens-Schönfelder, C., & Brenguier, F. (2019). Noise-based monitoring. In N. Nakata, L. Gualtieri, & A. Fichtner (Eds.), *Seismic ambient noise* (pp. 267–301). Cambridge University Press. https://doi.org/10.1017/9781108264808.011

Sens-Schönfelder, C., Pomponi, E., & Peltier, A. (2014). Dynamics of Piton de la Fournaise volcano observed by passive image interferometry with multiple references. *Journal of Volcanology and Geothermal Research*, *276*, 32–45. https://doi.org/10.1016/j.jvolgeores.2014.02.012

Sens-Schönfelder, C., Snieder, R., & Li, X. (2019). A model for nonlinear elasticity in rocks based on friction of internal interfaces and contact aging. *Geophysical Journal International*, *216*(1), 319–331. https://doi.org/10.1093/gji/ggy414

Sens-Schönfelder, C., & Wegler, U. (2006). Passive image interferemetry and seasonal variations of seismic velocities at Merapi Volcano, Indonesia. *Geophysical Research Letters*, *33*(21), 1–5. https://doi.org/10.1029/2006GL027797

Seropian, G., Kennedy, B. M., Walter, T. R., Ichihara, M., & Jolly, A. D. (2021). A review framework of how earthquakes trigger volcanic eruptions. *Nature Communications*, *12*(1), 1–13. https://doi.org/10.1038/s41467-021-21166-8

Seydoux, L., Balestriero, R., Poli, P., de Hoop, M., Campillo, M., & Baraniuk, R. (2020). Clustering earthquake signals and background noises in continuous seismic data with unsupervised deep learning. *Nature Communications*, *11*(1), 3972. https://doi.org/10.1038/s41467-020-17841-x

Shapiro, N., Sens-Schönfelder, C., Lühr, B., Weber, M., & Abkadyrov, I. (2015). Klyuchevskoy volcanic group experiment (kiss) [Dataset]. GFZ Data Services. https://doi.org/10.14470/K47560642124

Shapiro, N., Sens-Schönfelder, C., Lühr, B., Weber, M., Abkadyrov, I., Gordeev, E., et al. (2017). Understanding Kamchatka's extraordinary volcano cluster. *Eos*. https://doi.org/10.1029/2017EO071351

Silver, P. G., Daley, T. M., Niu, F., & Majer, E. L. (2007). Active source monitoring of cross-well seismic travel time for stress-induced changes. *Bulletin of the Seismological Society of America*, *97*(1B), 281–293. https://doi.org/10.1785/0120060120

Snieder, R. (2006). The theory of coda wave interferometry. *Pure and Applied Geophysics*, *163*(2–3), 455–473. https://doi.org/10.1007/s00024-005-0026-6

Snieder, R., & Hagerty, M. (2004). Monitoring change in volcanic interiors using coda wave interferometry: Application to Arenal Volcano, Costa Rica. *Geophysical Research Letters*, *31*(9). https://doi.org/10.1029/2004GL019670

Soubestre, J., Chouet, B., & Dawson, P. (2021). Sources of volcanic tremor associated with the summit caldera collapse during the 2018 east Rift eruption of Kīlauea volcano, Hawaii. *Journal of Geophysical Research: Solid Earth*, *126*(6), 1–33. https://doi.org/10.1029/2020jb021572

Soubestre, J., Seydoux, L., Shapiro, N. M., de Rosny, J., Droznin, D. V., Droznina, S. Y., et al. (2019). Depth migration of Seismovolcanic tremor sources below the klyuchevskoy volcanic group (kamchatka) determined from a network-based analysis. *Geophysical Research Letters*, *46*(14), 8018–8030. https://doi.org/10.1029/2019GL083465

Steinmann, R., Hadziioannou, C., & Larose, E. (2021). Effect of centimetric freezing of the near subsurface on Rayleigh and Love wave velocity in ambient seismic noise correlations. *Geophysical Journal International*, *224*(1), 626–636. https://doi.org/10.1093/gji/ggaa406

Steinmann, R., Seydoux, L., Beaucé, É., & Campillo, M. (2022). Hierarchical exploration of continuous seismograms with unsupervised learning. *Journal of Geophysical Research: Solid Earth*, *127*(1), 1–21. https://doi.org/10.1029/2021JB022455

Steinmann, R., Seydoux, L., & Campillo, M. (2022). AI-Based unmixing of medium and source signatures from seismograms: Ground freezing patterns. Manuscript submitted for publication. https://doi.org/10.1002/essoar.10510959.1

Taira, T., & Brenguier, F. (2016). Response of hydrothermal system to stress transients at Lassen Volcanic Center, California, inferred from seismic interferometry with ambient noise 4. Seismology. *Earth Planets and Space*, *68*(1), 162. https://doi.org/10.1186/s40623-016-0538-6

Takano, T., Nishimura, T., & Nakahara, H. (2017). Seismic velocity changes concentrated at the shallow structure as inferred from correlation analyses of ambient noise during volcano deformation at Izu-Oshima, Japan. *Journal of Geophysical Research: Solid Earth*, *122*(8), 6721–6736. https://doi.org/10.1002/2017JB014340

Tang, G., Clark, M. P., Papalexiou, S. M., Ma, Z., & Hong, Y. (2020). Have satellite precipitation products improved over last two decades? A comprehensive comparison of GPM IMERG with nine satellite and reanalysis datasets. *Remote Sensing of Environment*, *240*(September 2019), 111697. https://doi.org/10.1016/j.rse.2020.111697

Taran, Y. A. (2009). Geochemistry of volcanic and hydrothermal fluids and volatile budget of the Kamchatka-Kuril subduction zone. *Geochimica et Cosmochimica Acta*, *73*(4), 1067–1094. https://doi.org/10.1016/j.gca.2008.11.020

Tozer, B., Sandwell, D. T., Smith, W. H., Olson, C., Beale, J., & Wessel, P. (2019). Global bathymetry and topography at 15 arc sec: Srtm15+. *Earth and Space Science*, *6*(10), 1847–1864. https://doi.org/10.1029/2019EA000658

Uieda, L., Tian, D., Leong, W. J., Jones, M., Schlitzer, W., Grund, S., et al. (2022). PyGMT: A Python interface for the Generic Mapping Tools [Software]. Zenodo. https://doi.org/10.5281/zenodo.7481934

Van Den Abeele, K. E.-A. (2002). Influence of water saturation on the nonlinear elastic mesoscopic response in Earth materials and the implications to the mechanism of nonlinearity. *Journal of Geophysical Research*, *107*(B6), 1–11. https://doi.org/10.1029/2001jb000368

Viens, L., Denolle, M. A., Hirata, N., & Nakagawa, S. (2018). Complex near-surface rheology inferred from the response of greater Tokyo to strong ground motions. *Journal of Geophysical Research: Solid Earth*, *123*(7), 5710–5729. https://doi.org/10.1029/2018JB015697

Viens, L., & Van Houtte, C. (2020). Denoising ambient seismic field correlation functions with convolutional autoencoders. *Geophysical Journal International*, *220*(3), 1521–1535. https://doi.org/10.1093/gji/ggz509

Walter, T. R., & Amelung, F. (2007). Volcanic eruptions following M 9 megathrust earthquakes: Implications of the Sumatra-Andaman volcanoes. *Geology*, *35*(6), 539–542. https://doi.org/10.1130/G23429A.1

Wang, Q. Y., Brenguier, F., Campillo, M., Lecointre, A., Takeda, T., & Aoki, Y. (2017). Seasonal crustal seismic velocity changes throughout Japan. *Journal of Geophysical Research: Solid Earth*, *122*(10), 7987–8002. https://doi.org/10.1002/2017JB014307

Ward, J. H. J. (1963). Hierarchical grouping to optimize an objective function. *Journal of the American Statistical Association*, *58*(301), 236–244. https://doi.org/10.1080/01621459.1963.10500845

Watt, S. F., Pyle, D. M., & Mather, T. A. (2009). The influence of great earthquakes on volcanic eruption rate along the Chilean subduction zone. *Earth and Planetary Science Letters*, *277*(3–4), 399–407. https://doi.org/10.1016/j.epsl.2008.11.005

Wegler, U., Nakahara, H., Sens-Schönfelder, C., Korn, M., & Shiomi, K. (2009). Sudden drop of seismic velocity after the 2004 Mw 6.6 mid-Niigata earthquake, Japan, observed with Passive Image Interferometry B06305. *Journal of Geophysical Research*, *114*(6), 1–11. https://doi.org/10.1029/2008JB005869

Wegler, U., & Sens-Schönfelder, C. (2007). Fault zone monitoring with passive image interferometry. *Geophysical Journal International*, *168*(3), 1029–1033. https://doi.org/10.1111/j.1365-246X.2006.03284.x

Yates, A., Caudron, C., Lesage, P., Mordret, A., Lecocq, T., & Soubestre, J. (2022). Assessing similarity in continuous seismic cross-correlation functions using hierarchical clustering: Application to Ruapehu and Piton de la Fournaise volcanoes. *Geophysical Journal International*, *233*(1), 472–489. https://doi.org/10.1093/gji/ggac469

Yates, A., Savage, M., Jolly, A., Caudron, C., & Hamling, I. (2019). Volcanic, coseismic, and seasonal changes detected at white island (whakaari) volcano, New Zealand, using seismic ambient noise. *Geophysical Research Letters*, *46*(1), 99–108. https://doi.org/10.1029/2018GL080580

Yogodzinski, G. M., Lees, J. M., Churikova, T. G., Dorendorf, F., Wöerner, G., & Volynets, O. N. (2001). Geochemical evidence for the melting of subducting oceanic lithosphere at plate edges. *Nature*, *409*(6819), 500–504. https://doi.org/10.1038/35054039